Influence of geochemical features on the mechanical properties of organic matter in shale

Junliang Zhao[1], Wei Zhang[1], Dongxiao Zhang[2], Ren Wei[3], and Yuhan Wang[3]

[1]BIC-ESAT, ERE and SKLTCS, College of Engineering, Peking University, Beijing 100871, P. R. China.

[2]School of Environmental Science and Engineering, Southern University of Science and Technology, Shenzhen 518055, P. R. China.

[3]School of Earth and Space Sciences, Peking University, Beijing 100871, P. R. China.

Corresponding author: Dongxiao Zhang (zhangdx@sustech.edu.cn)

Key Points:

- Young's modulus of inertinite and vitrinite is much higher than that of bitumen
- Modulus of organic matter increases with thermal maturity
- Intensity ratio of D peak to G peak of inertinite's Raman spectrum exhibits a decreasing trend with maturity

Abstract

Organic matter is an important constituent in organic-rich shale, which influences the hydrocarbon generation, as well as the mechanical behavior, of shale reservoirs. The physical, chemical, and mechanical properties of organic matter depend on the source material and the thermal evolution process. Previous works attempted to investigate the impact of thermal maturation on the mechanical properties of organic matter. However, owing to the lack of maceral classification and the limitation of data volume during the mechanical measurement, no consistent trend has been identified. In this work, vitrinite reflectance test, scanning electron microscope observation, nanoindentation, and micro-Raman analysis were combined for geochemical and mechanical characterization. A total of 114 test areas were selected for testing, enhancing reliability of the test results. The Young's moduli of organic matter are from 3.57 GPa to 8.32 GPa. With the same thermal maturity, inertinite has the highest Young's modulus, while the modulus of bitumen is the lowest. The Young's moduli of different organic types all increase with vitrinite reflectance. When vitrinite reflectance increases from 0.62% to 1.13%, the modulus of inertinite and vitrinite is increased by 57% and 78%, respectively. The indentation creep of different organic matter suggests that the stiffer organic type demonstrates less creep influence. In addition, with the increase of thermal maturity, the micro-Raman test results show a decrease of intensity ratio of D peak to G peak, indicating an increase of the ordered structure in organic matter. From the characterization results, it was found that organic type and thermal maturity reflect the diversity of the source material and the chemical structure change during the thermal evolution process, and together they influence the mechanical properties of organic matter.

Keywords: organic type; thermal maturity; organic matter; Young's modulus; shale.

1. Introduction

Organic-rich shale is not only the source rock of conventional reservoirs, but also the reservoir rock of shale oil/gas reservoirs. Organic matter is an important constituent in organic-rich shale, which distinguishes organic-rich shale from other mud rocks with low organic content, and significantly influences the exploration and development of shale oil/gas. On the one hand, kerogen is the source material of hydrocarbon, and total organic carbon (TOC) content is an essential index for the evaluation of geological sweet spots (Cudjoe et al., 2016; Naizhen and Guoyong, 2016). On the other hand, the mechanical properties that significantly affect the fracturing effect of shale are quite different for organic matter and inorganic minerals in shale. Consequently, many indices for the evaluation of engineering sweet spots, for example, the brittleness index (Rybacki et al., 2016; Wang and Carr, 2012; Zhao et al., 2018), are also related to organic matter.

Organic matter in shale comes from deposits of the dead bodies of ancient organisms, and it can be classified on the basis of the diversity of source organisms and sedimentary environments. According to solubility, organic matter can be divided into kerogen and bitumen (Hunt, 1979). Regarding kerogen, two classification schemes exist: optical classification and chemical classification. The optical classification scheme borrows methods and concepts from coal petrology (Hutton et al., 1994; Stach et al., 1982). Through reflected light analysis, kerogen can be classified into maceral groups, such as inertinite, vitrinite, and exinite. Chemical classification focuses on the content of C, H, and O elements in kerogen. By major chemical elements analysis, kerogen can be classified as type I, type II, and type III (Tissot and Welte, 2013). Optical classification and chemical classification schemes are related to each other (Hunt, 1979). However, optical classification usually measures organic matter in certain micro regions, while

chemical classification refers to characterization of the whole rock. In addition to organic type, thermal maturity constitutes another important geochemical property of organic matter. Thermal maturity indicates the thermal evolution and hydrocarbon generation stage of the source rock. Vitrinite reflectance is a key indicator of thermal maturity. Owing to the absence of higher plants, rocks prior to the Devonian period do not contain vitrinite. Consequently, researchers usually measure the reflectance of bitumen or graptolite as an alternative (Bertrand, 1990; Bertrand and Heroux, 1987; Jacob, 1989). Organic type and thermal maturity together influence the chemical structures of organic matter in shale.

Due to the lack of resolution, the elastic property of organic matter is difficult to characterize using conventional mechanical test methods. However, micromechanical test techniques, such as nanoindentation and modulus mapping based on nanoindenter and PeakForce quantitative nanomechanical mapping (QNM) by atomic force microscope (AFM), offer convenience of investigation at micro scale (Balooch et al., 2004; Dayal et al., 2009; Dokukin and Sokolov, 2012). Mechanical characterization of organic matter in shale can be divided into two types. In the first type, organic matter was treated as a part of the main constituents in shale, and was directly characterized through the application of micromechanical test techniques (Alstadt et al., 2015; Bennett et al., 2015; Eliyahu et al., 2015; Kumar et al., 2012; Wilkinson et al., 2015; Zargari et al., 2013; Zeszotarski et al., 2004). The reported modulus of organic matter was generally between 0 GPa to 25 GPa, which was much lower than that of inorganic minerals. These researches revealed strong micromechanical heterogeneity within different constituents in organic-rich shales. In the second type, geochemical features of organic matter were taken into consideration (Emmanuel et al., 2016; Li et al., 2018; Zargari et al., 2016). Kerogen and bitumen with different thermal maturities were usually separated during the measurements. Previous

works in the second type suggested that the elastic modulus of organic matter is associated with organic type and thermal maturity. Owing to the lack of classification of kerogen and the limitation of data volume, however, no consistent trend has yet been discerned. Yang et al. (2017) measured the mechanical properties of different macerals in shale using AFM-based Nano IR. Inertinite, bitumen and tasmanite were separated in the work, but thermal maturity was not considered for mechanical characterization. Similar to characterization of organic matter in shale, the mechanical properties of macerals in coal and the influence of coal rank have also been studied (Borodich et al., 2015; Epshtein et al., 2015; Vranjes et al., 2018; Zhang et al., 2019). However, understanding of the exact influence requires further studies. In addition, molecular simulation has recently been utilized to investigate the structures and mechanical properties of organic matter (Bousige et al., 2016; Tong et al., 2016; Ungerer et al., 2014). The chemical structure of organic matter is very complex, and to precisely construct a molecular model, and predict the physical and mechanical properties, remain a challenge. Experimental works at micro and nano scales can provide a useful reference and validation for simulations.

In this study, four shale samples with different thermal maturities from the Bonan Sub-sag are prepared. A number of geochemical and micromechanical tests are combined to characterize the properties of organic matter in each sample. Vitrinite reflectance is measured using a photomicrometer. Inertinite, vitrinite, and bitumen are identified based on an optical classification scheme. Nanoindentation is performed to characterize the mechanical properties of organic matter in the selected test areas. Moreover, to elucidate the evolution of chemical structures of organic matter, micro-Raman test is carried out. Micromechanical test results are compared with the reported data. The influence of organic type and thermal maturity is discussed on the basis of the characterization results.

2. Materials and methods

2.1. Sample information and preparation

Samples used in this study are shale cores of the third member of the Shahejie Formation from the Bonan Sub-sag. The Bonan Sub-sag is a third-order tectonic unit in the central part of the Zhanhua Depression in the Bohai Bay Basin with an area of 600 km^2. During the Paleogene period, the Bohai Bay Basin experienced initial, developmental, prosperous and atrophic periods of the fault depression, and successively developed the Kongdian Formation, the Shahejie Formation, and the Dongying Formation (Jiu et al., 2013; Wang et al., 2015). The Shahejie Formation can be divided into four sub-sections, and the third member of the Shahejie Formation from the Bonan Sub-sag contains a large number of shale oil formations.

Shale pieces with thicknesses from 2 mm to 5mm were cut from the shale cores. Then, mechanical polishing was performed to keep the upper and lower surface of the shale pieces parallel to each other, and to primarily decrease surface roughness. Finally, the upper surface was subjected to ion polishing to further decrease roughness. The roughness of a 20 μm × 20 μm area in the sample surface is below 100 nm.

2.2. Characterization methods

2.2.1. Vitrinite reflectance test

The vitrinite reflectance test is an effective method to characterize the thermal maturity of organic matter. The device for the vitrinite reflectance test, the photomicrometer, is a combination of an optical microscope and a spectrophotometer. The optical microscope with an oil immersion objective is utilized for observation and test area selection. The spectrophotometer is used to measure reflectance in a certain area. In addition to the vitrinite reflectance test, a

photomicrometer can also assist with optical classification of organic types according to image contrast and reflectance data. The reflectance test and optical microscope observation, which determine thermal maturity and organic type, constitute the foundation of the following tests.

2.2.2. Micro-Raman test

Raman spectrum is very sensitive to the structure and molecular arrangement of carbon materials. Raman spectrum analysis is widely employed for characterization of carbon materials, such as carbon nanotube and graphene (Dresselhaus et al., 2005; Ferrari et al., 2006; Pimenta et al., 2007). Numerous researchers have also performed Raman spectrum tests on organic matter in source rocks, and attempted to correlate the spectrum features with the results from conventional vitrinite reflectance tests, to develop novel methods for the determination of thermal maturity (Kelemen and Fang, 2001; Wilkins et al., 2014). Two ways of Raman spectrum analysis exist for organic matter in shale. The first one needs to extract organic matter from shale rocks by mechanical and chemical purification methods. However, this way necessitates destruction of the shale rock during purification, which makes it unusable for mechanical tests. The second way is via a micro-Raman test. Similar to the photometric test, micro-Raman combines optical observation and Raman spectrum analysis (Lünsdorf, 2016; Tselev et al., 2014), which can locate the micro areas and perform the measurements. Due to its advantages, the second way is chosen for this study.

2.2.3. Nanoindentation

Mainstream commercial nanoindenters are developed on the basis of the method proposed by Oliver and Pharr (Oliver and Pharr, 1992; Oliver and Pharr, 2004). During the nanoindentation measurement, an indenter with a certain geometry is penetrated into the sample surface until the

156 targeted force or depth, and then it is pulled out. The load P on the sample and the displacement
157 h of the indenter tip are recorded in the loading, holding, and unloading process (Figure 1).

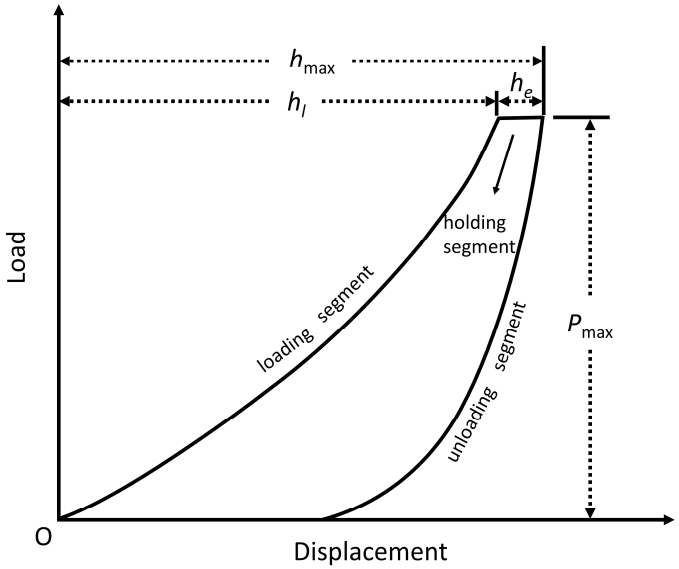

158

159 **Figure 1.** A schematic representation of load-displacement curve from nanoindentation. P_{max} is
160 the peak load; h_{max} is the maximum indenter displacement; h_l is the displacement at the end of
161 the loading segment; and h_e is the displacement increase during the holding process.

162 The unloading segment of the *P*-*h* curve reflects the elastic properties of the sample material.
163 According to the contact mechanics (Pharr et al., 1992), the basic model for nanoindentation is as
164 follows:

165 $$E_r = \frac{\sqrt{\pi}}{2}\frac{S}{\sqrt{A}} \tag{1}$$

166 where E_r is the reduced modulus; S is the slope of the initial unloading segment; and A is the
167 contact area of the indenter tip on the sample surface, which can be determined by the corrected
168 area function (Oliver and Pharr, 1992):

169 $$A = 24.5h_c^2 + \sum_{i=0}^{7} C_i h_c^{1/2^i} \tag{2}$$

where C_i are fitting parameters; and h_c is the contact depth of the indenter, which is related to the maximum displacement $h_{\max}$ (Oliver and Pharr, 1992):

$$h_c = h_{\max} - \beta \frac{P_{\max}}{S} \tag{3}$$

where β is the parameter corresponding to the geometry of the indenter; and $P_{\max}$ is the peak load. The reduced modulus is determined by both the sample and the indenter material. The following equation can be used to eliminate the influence from the indenter and calculate the Young's modulus E of the sample (Johnson, 1987):

$$\frac{1-\gamma^2}{E} = \frac{1}{E_r} - \frac{1-\gamma_{tip}^2}{E_{tip}} \tag{4}$$

where γ is the Poisson's ratio of the sample; and E_{tip} and γ_{tip} are the Young's modulus and Poisson's ratio of the indenter tip, respectively.

2.2.4. Experimental procedures

Geochemical test and mechanical characterization are combined in this study (Figure 2). Ion-polished samples were placed into a photomicrometer (QDI 302, CRAIC; DM4500P, Leica). Test areas containing organic matters were observed and selected under an oil immersion objective (Figure 2a). The spectrophotometer was used to measure the reflectance of organic matter. The illumination spot size for reflectance measurement was approximately 3 μm. Organic type was identified through optical image and reflectance data. Vitrinite reflectance constitutes the measurement of the thermal maturity of each sample. SEM observation (Figure 2b) was then carried out to observe the selected test areas at a low vacuum condition with an accelerate voltage of 15 kV (Quanta 200F, FEI). For convenience of positioning in the following procedures, the precise coordinate of each test area was recorded, and SEM images of organic matters were captured at various magnifications. Subsequently, the elastic properties of organic

matter in each sample were measured using nanoindentation (Tribo Indenter 950, Hysitron). Scanning probe microscopy (SPM) was performed prior to (Figure 2c) and after (Figure 2e) nanoindentation, to determine the indentation position and to observe the residual indentation, respectively. The indentation was usually placed at the center position of organic matter to avoid the interference from surrounding minerals. A Berkovich diamond indenter with a nominal tip radius of 100 nm was chosen for the test. Under load controlling mode, the maximum load was set to be 1000 μN (Figure 2d), which was uniform for each indentation. The loading, holding, and unloading time were set to be 10 s, 2 s and 10 s, respectively. The contact area of the indentation was on the order of 10^6 nm^2. Finally, the micro-Raman test (Figure 2f) was performed to elucidate the structural variation within the organic matter with different thermal maturities (DXRxi, ThermoFisher). The immersion source was a 532 nm laser, and the exposure time was 0.05 s. The spot size of the laser beam was about 1 μm. To decrease damage on the sample surface, the laser power was set to be 0.5 mW.

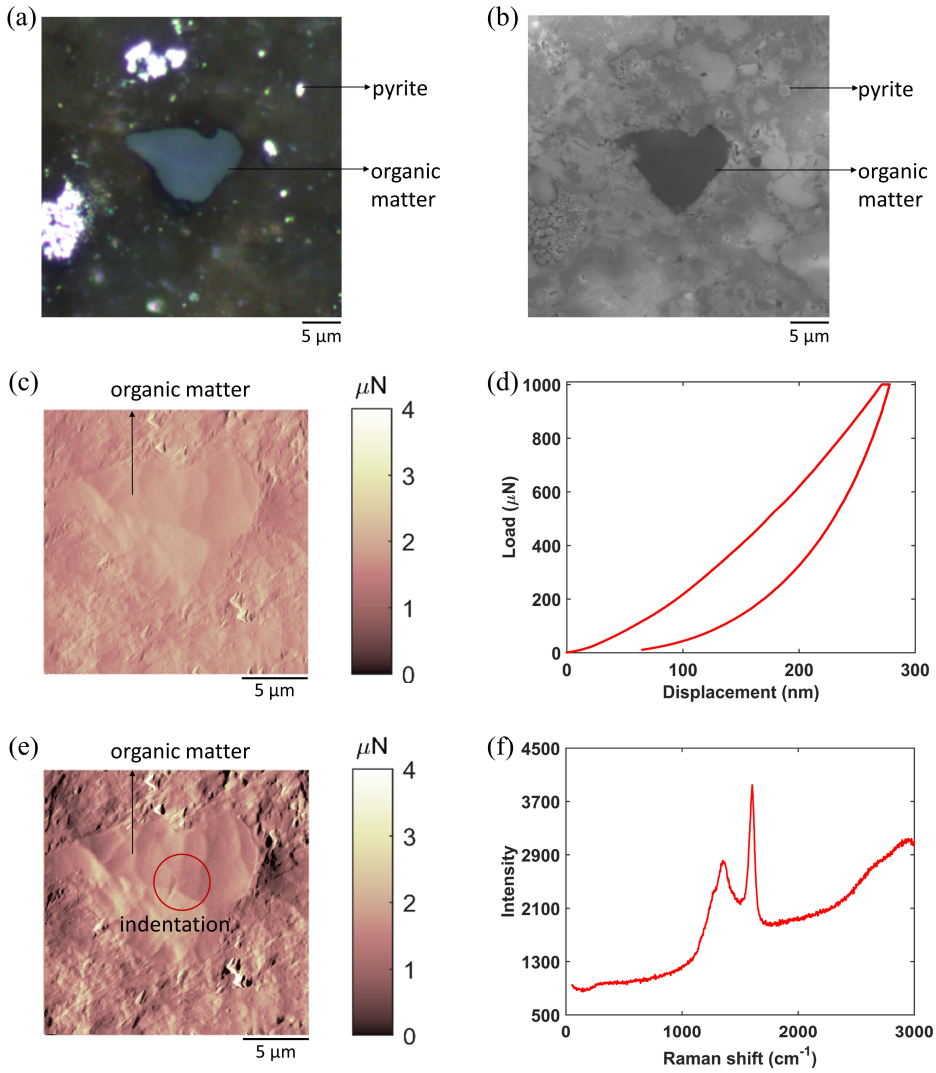

Figure 2. Experimental procedures: (a) Vitrinite reflectance test, macerals classification, and test area selection; (b) SEM observation and test area location; (c) SPM (scanning frequency = 0.2 Hz) observation prior to nanoindentation; (d) nanoindentation; (e) SPM (scanning frequency = 0.5 Hz) observation after nanoindentation; and (f) micro-Raman analysis.

3. Results and discussion

3.1. Organic type and thermal maturity

Table 1 shows the organic type classification and thermal maturity test results. The vitrinite reflectance of shale samples is from 0.62% to 1.13%, which means that all of the samples are in

the mature stage. According to the image features under the oil immersion objective, three organic types, including vitrinite, inertinite and bitumen, are identified in the shale samples.

Table 1. Vitrinite reflectance and number of areas tested in each sample.

Sample	R_o (%)	Number of areas tested		
		Vitrinite	Inertinite	Bitumen
J1	0.62	16	11	——
J2	0.69	12	9	15
J3	0.94	10	11	6
J4	1.13	9	12	3

Figure 3 compares the optical images and SEM images of different organic types. Compared with the dry objective, the oil immersion objective can greatly increase the image contrast and the clarity of organic matter. Through the first column of Figure 3, one can see that the image features of the typical test areas are markedly different. Specifically, the organic type in the first test area is inertinite, which is cinerous and seems to protrude from the sample surface (Figure 3a). In contrast, vitrinite in the second test area (Figure 3c) and bitumen in the last test area (Figure 3e) are dark gray and brown, respectively. However, it is challenging to differentiate the organic types based only on the image contrast of SEM images (Figure 3b, d, f). In addition to optical images, the reflectance test results can also assist with the classification of organic type. The reflectance of vitrinite is usually higher than the reflectance of bitumen, while lower than that of inertinite. In sample J2, for example, bitumen reflectance is from 0.39% to 0.52%, vitrinite reflectance is from 0.46% to 1.1%, and inertinite reflectance is from 1.1% to 2.2%. A total of 114 test areas that contain different types of organic matter are selected for nanoindentation test (Table 1).

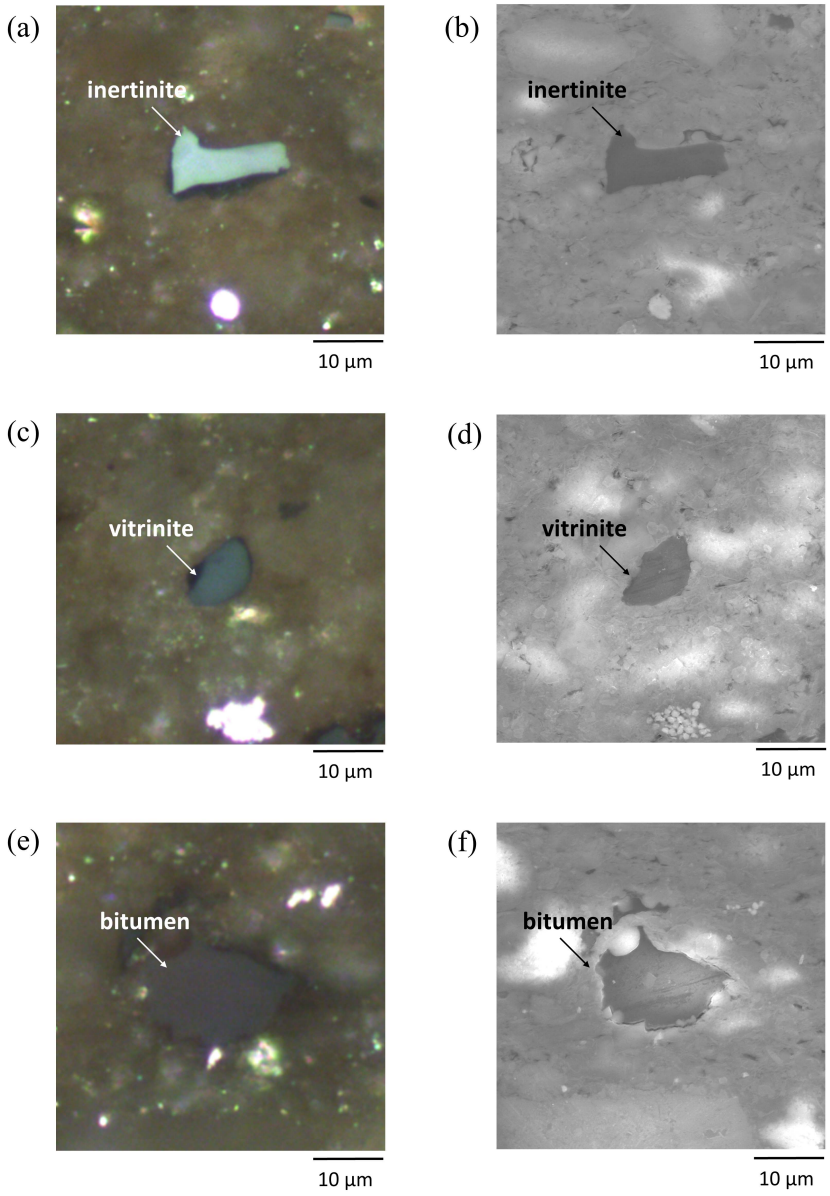

232

233 **Figure 3.** Different types of organic matter in sample J3: (a) Optical image and (b) SEM image
234 of inertinite; (c) optical image and (d) SEM image of vitrinite; and (e) optical image and (f) SEM
235 image of bitumen.

236 3.2. Nanoindentation results

237 The number of areas tested of each kind of organic matter in each sample is listed in Table 1.
238 Figure 4 assembles the *P-h* curves for different kinds of organic matter in each sample. With the

same maximum load setting, the maximum displacement of vitrinite is generally lower than that of inertinite, while higher than that of bitumen. The sudden increase of displacement during the loading process in Figure 4c, which is marked with a black circle, is termed *pop-in*. It suggests the rapture of organic matter. The comparison of the *P-h* curves indicates that bitumen is much softer than vitrinite and inertinite with the same thermal maturity.

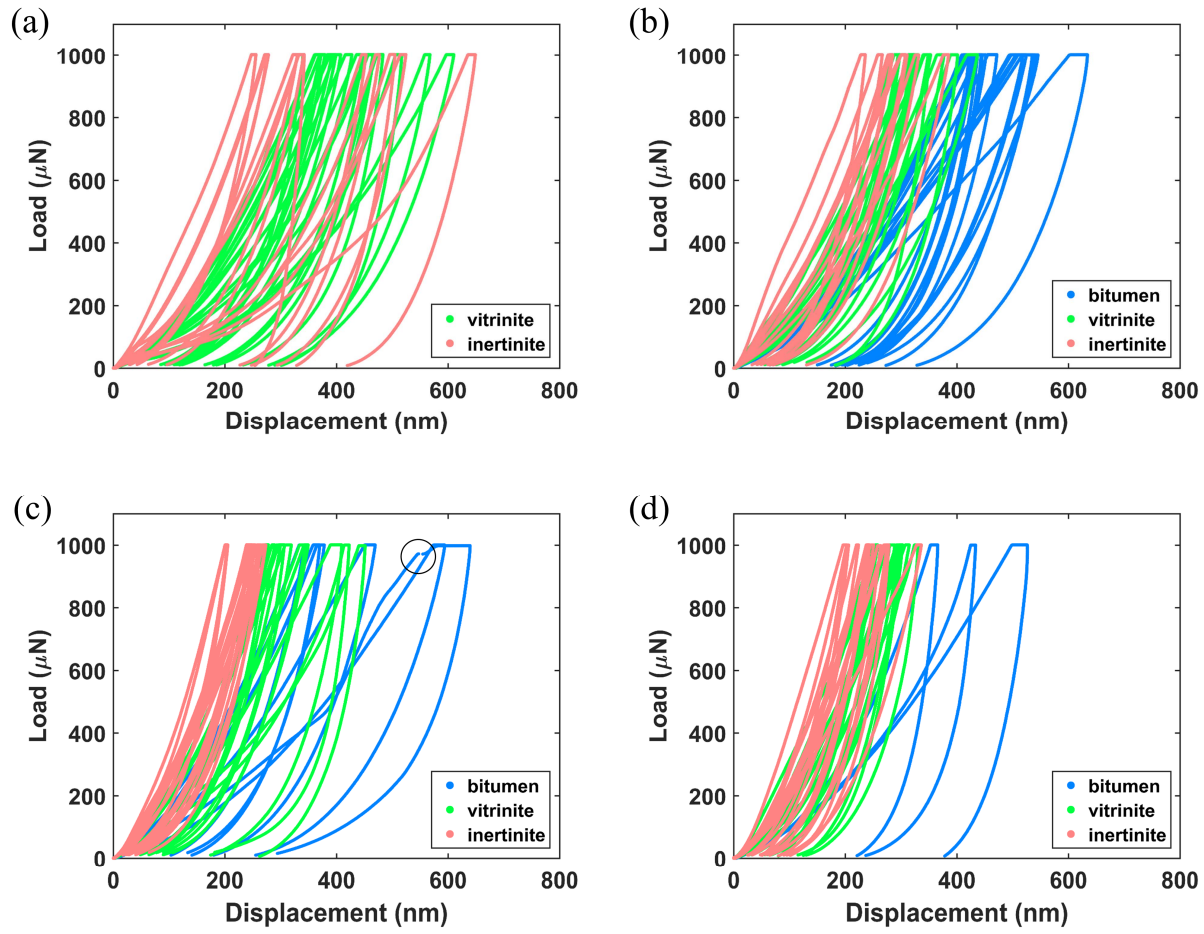

Figure 4. Assembly of representative *P-h* curves from sample J1 (a), J2 (b), J3 (c), and J4 (d).

The Young's modulus can be calculated using equation (1) to equation (4). The Young's modulus and Poisson's ratio of the diamond indenter tip are 1141 GPa and 0.07, respectively. However, the Poisson's ratio of organic matter remains unknown, and the estimation of Poisson's ratio influences the calculation results. A wide range of Poisson's ratio of organic

matter, from 0.05 to 0.45, was used in previous literature (Ahmadov et al., 2009; Eliyahu et al., 2015; Emmanuel et al., 2016; Li et al., 2018). Figure 5 illustrates the sensitivity to Poisson's ratio based on the load-displacement data in this work. The calculated Young's modulus of organic matter gradually increases with the selected Poisson's ratio value. In the following discussions, the Poisson's ratio of organic matter is assumed to be 0.3. The maximum uncertainty introduced by the assumption is approximately 12.4%.

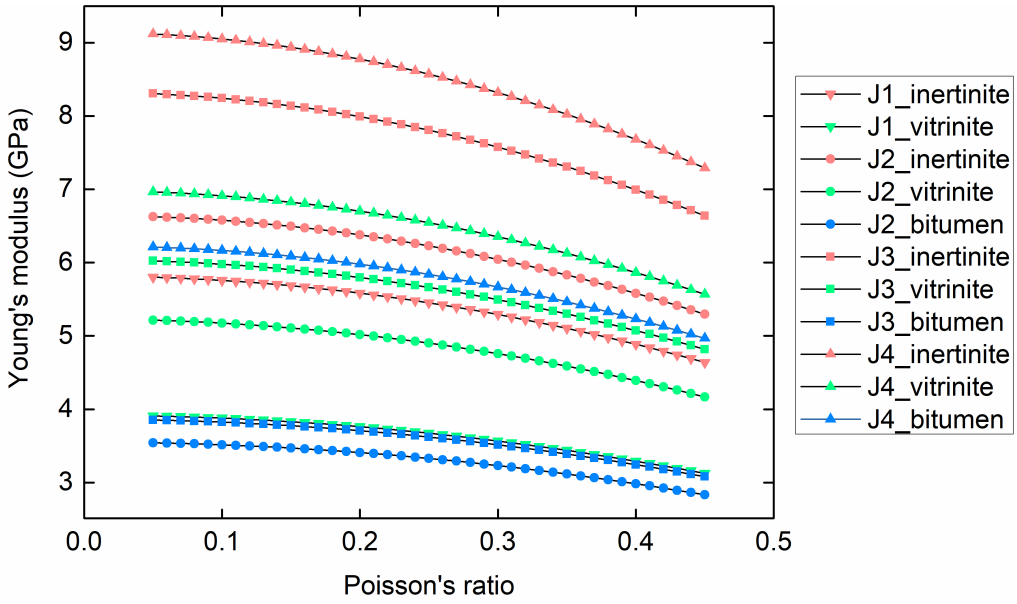

Figure 5. The sensitivity of calculated Young's modulus to Poisson's ratio of organic matter.

Table 2 summarizes Young's modulus calculation results. It is obvious that inertinite has the highest Young's modulus, while the modulus of bitumen is the lowest. Moreover, the Young's moduli of different organic types all increase with vitrinite reflectance. When vitrinite reflectance increases from 0.62% to 1.13%, the Young's modulus of inertinite increases from 5.29 GPa to 8.32 GPa, by 57%, and the Young's modulus of vitrinite increases from 3.57 GPa to 6.35 GPa, by 78%. From Table 2, it can be concluded that both organic type and thermal maturity affect the mechanical properties of organic matter. Repeated testing on a number of test areas (Table 1) for different organic types in each sample provides a valuable dataset to examine

the variability of the mechanical properties and the reliability of the test results. Except for a couple of test results (i.e., inertinite for sample J1 and bitumen for J3), the standard deviation for each type of testing is moderate (Table 2), indicating either a reliable testing result or moderate variability, or both.

Table 2. Young's modulus of different types of organic matter.

Sample	R_o (%)	Young's modulus (GPa) [a]		
		Vitrinite	Inertinite	Bitumen
J1	0.62	3.57±0.83	5.29±2.85	——
J2	0.69	4.76±0.85	6.05±1.63	3.23±0.80
J3	0.94	5.50±0.80	7.58±1.38	3.52±1.25
J4	1.13	6.35±0.97	8.32±1.53	5.67±0.84

[a]± indicates the standard deviation.

An increase in displacement in the holding segment (Figure 4) indicates the viscoelasticity of organic matter, which was also investigated in previous works (Epshtein et al., 2015; Liu et al., 2019; Zeszotarski et al., 2004). To discuss the problem, indentation creep C_{IT} is calculated by using the following equation (ISO14577-1, 2002):

$$C_{IT} = \frac{h_e}{h_l} \times 100 \tag{5}$$

where h_e and h_l are the displacement increase during the holding and loading process, respectively. The C_{IT} values of different types are summarized in Table 3. With the same maximum load and holding time setting, the indentation creep of bitumen is much higher than that of vitrinite and inertinite. The calculation results suggest that the stiffer organic type demonstrates less creep influence. However, no clear relation is identified between indentation creep and thermal maturity. While this work focuses on the elastic properties of organic matter, a longer holding time and more suitable test method, for example, dynamic mechanical analysis,

would be required for rigorous study of the creep behavior (Chagnon et al., 2013; Koch et al., 2007).

Table 3. Indentation creep calculation results.

Sample	R_o (%)	Indentation creep (%) [a]		
		Vitrinite	Inertinite	Bitumen
J1	0.62	2.40±0.31	2.21±0.62	——
J2	0.69	3.09±0.73	2.65±0.81	4.61±1.11
J3	0.94	2.97±1.00	2.18±0.51	4.66±2.87
J4	1.13	2.38±0.75	2.18±0.59	3.77±1.76

[a]± indicates the standard deviation.

3.3. Micro-Raman analysis

Because of the influence from fluorescence, the Raman spectrum of bitumen and vitrinite has a poor signal-to-noise ratio, and we can only obtain reliable data about inertinite. Through processing of the original spectrum, the micro-Raman test results are analyzed. Figure 6 illustrates a typical Raman spectrum of inertinite. There is a strong fluorescence background in the original Raman data (Figure 6a). Similar to the carbon materials, two characteristic peaks in the spectrum are observed. To remove the background, the baseline is calculated by using the data points around the characteristic peaks. In Figure 6b, the peak around 1350 cm^{-1} is the defect peak (D peak), which indicates the defects and the disordered structure in the material. The peak around 1600 cm^{-1} is the graphene peak (G peak), which originates from the plane structure of carbon materials. The intensity ratio of D peak to G peak (IR (D/G)) can be the indicator of the degree of graphitization. A higher IR (D/G) indicates fewer defects, a smaller disordered structure, and a higher degree of graphitization.

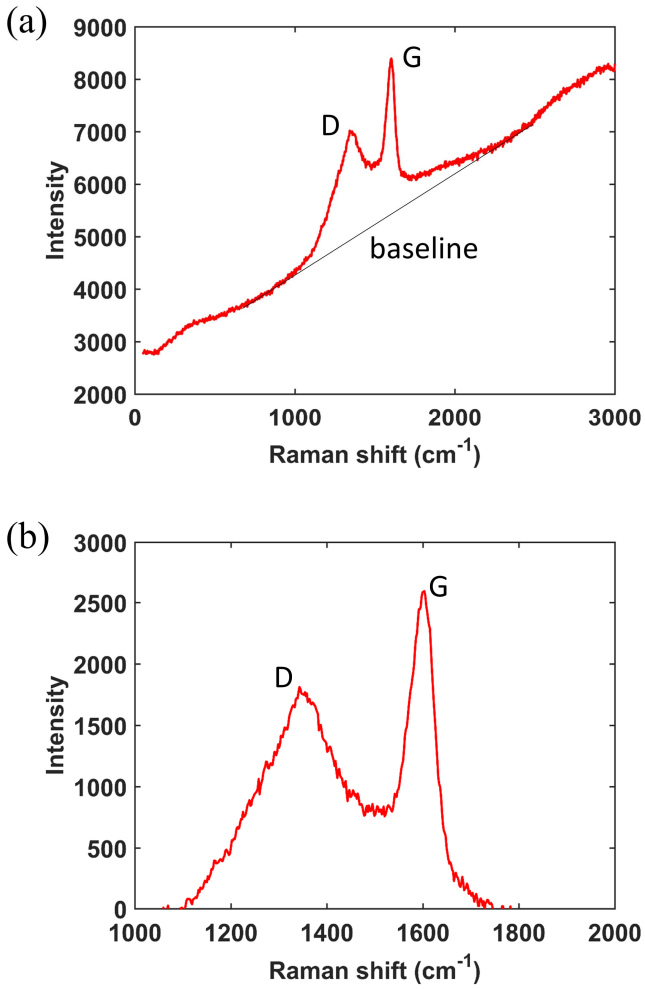

Figure 6. Data processing of Raman spectrum: (a) Original Raman spectrum of inertinite with strong fluorescence background; and (b) processed spectrum in the region of interest. D and G indicate characteristic peaks in the Raman spectrum of carbon material. The baseline is calculated by using the data points around the characteristic peaks. The intensity ratio of D peak to G peak is calculated through the division of maximum intensity value of the D band to that of the G band.

Figure 7 compares two representative Raman spectrums from sample J1 and J4, respectively. The IR (D/G) of the inertinite in sample J1 is higher than that of the inertinite in

311 sample J4, which suggests that the organic matter in sample J4 has a higher degree of
312 graphitization. The IR (D/G) of each sample is averaged (Table 4) in consideration of the
313 heterogeneity within different inertinites in a certain shale sample. When vitrinite reflectance
314 increases, the IR (D/G) exhibits a general decreasing trend. The chemical structure change
315 results from thermal evolution. With the increase of thermal maturity, the aliphatic structure is
316 gradually decomposed, and the aromaticity of kerogen increases (Craddock et al., 2018; Duan et
317 al., 2018; Tissot and Welte, 2013). Therefore, the calculation results reveal that the organic
318 matter with a higher thermal maturity may contain fewer defects and a more ordered structure.

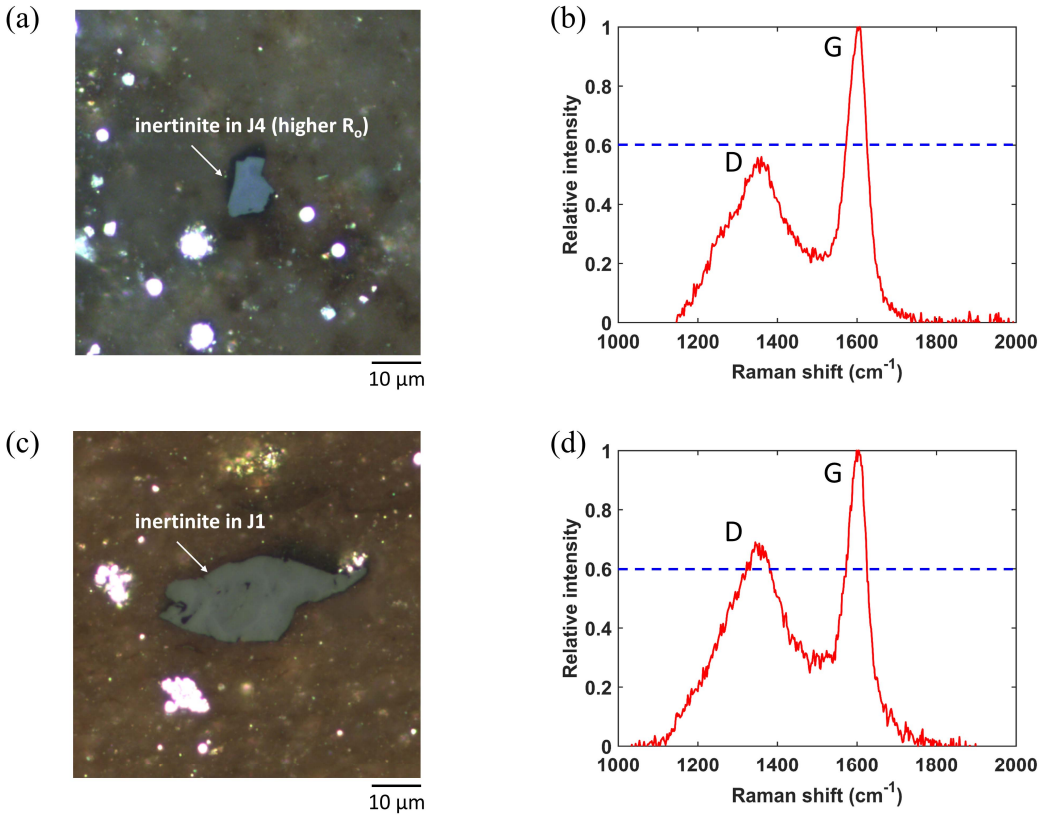

319

320 **Figure 7.** Representative inertinite area and corresponding Raman spectrum from sample J4 (a,
321 b) and J1 (c, d).

322

Table 4. Intensity ratio of D peak to G peak of different samples.

Sample	R_o (%)	IR (D/G) [a]	Number of areas tested
J1	0.62	0.648±0.024	11
J2	0.69	0.667±0.022	9
J3	0.94	0.620±0.038	11
J4	1.13	0.600±0.034	12

[a]± indicates the standard deviation.

3.4. Comparison with extant literature

Table 5 presents a comparison of the test results in this study and the reported data. In previous works, utilization of dynamic test techniques is preferred for mechanical characterization, including modulus mapping by nanoindentation system and QNM by AFM. Kerogen and bitumen are distinguished in previous research, but the macerals are not classified. Although Zargari et al. (2016) and Li et al. (2018) both investigate organic matter in Bakken shale, the test results show different trends. Zargari et al. (2016) find the modulus reduction of kerogen from immature to mature stage, while Li et al. (2018) observe that organic matter becomes stiffer as thermal maturity increases. The different findings may be owing to the lack of classification of organic type and the limited data volume. The test results provided by Zargari et al. (2016) are storage moduli, which are measured by using modulus mapping with a diamond indenter. Storage modulus is comparable to reduced modulus, and is also influenced by both the sample and the indenter tip (Zhao et al., 2018). The relation between storage modulus and Young's modulus is in the same form as equation (4) (Syed Asif et al., 2001), and the Young's modulus of diamond is much higher than that of organic matter. Thus, storage modulus and converted Young's modulus should have the same trend from immature to mature stage. The conclusion by Emmanuel et al. (2016) is that the modulus of kerogen significantly increases when vitrinite

343 reflectance increases from 0.40% to 0.82%, while the modulus hardly changes when vitrinite
344 reflectance increases from 0.82% to 1.25%. However, in this paper, we find that the elastic
345 modulus of vitrinite, inertinite, and bitumen all increase with thermal maturity.

346 Different from the previous investigations listed in Table 5, this study considers the
347 influence of not only thermal maturity, but also organic type. Vitrinite and inertinite are
348 identified based on optical microscope images and reflectance data. The difference of elastic
349 properties between vitrinite and inertinite are found by nanoindentation measurements.
350 Consequently, without consideration of maceral classification, conclusions about the influence
351 from thermal maturity may be unreliable, especially when the data volume is limited. In addition,
352 most of the previous investigations divide the shale samples into two parts. One is for
353 geochemical characterization, while the other one is for the mechanical test. Sample-to-sample
354 variation is also not adequately considered. In this work, a set of geochemical-mechanical
355 experiments is performed on the same selected test areas in a certain sample. Sample-to-sample
356 variation no longer presents a problem, and the experimental data of repeated tests on the same
357 type of test areas provide meaningful statistics. Finally, micromechanical tests on shale are very
358 time consuming, due to the complexity of sample preparation and locating the test area. The
359 number of areas tested in previous works is also relatively small. Here, the data volume is
360 significantly increased, which makes the test results in this work more reliable.

361

362

363

364

365

366

367 **Table 5.** Comparison with the test results in previous works.

Reference	R_o (%)	Modulus (GPa)			Test technique	Number of areas tested
		Kerogen		Bitumen		
		Vitrinite	Inertinite			
Zargari et al. (2016)[a]	Immature	15~20		——	Modulus mapping	12
	Mature	7~10		——		
	Mature	7~10		——		
	Overmature	7~12		——		
Emmanuel et al. (2016)[b]	0.40	6.10		——	AFM	26
	0.82	16.0		7.50		
	1.25	15.80		8.50		
Li et al. (2018)[c]	0.35	2.91		——	AFM	3
	0.64	——		3.33		
	1.04	——		11.77		
This work[d]	0.62	3.57	5.29	——	Nano-indentation	114
	0.69	4.76	6.05	3.23		
	0.94	5.50	7.58	3.52		
	1.13	6.35	8.32	5.67		

368 [a]Modulus in this literature is storage modulus;
369 [b]Modulus in this literature is Young's modulus;
370 [c]Modulus in this literature is Young's modulus;
371 [d]Modulus in this work is Young's modulus.
372

373 **4. Conclusions**

374 In the present paper, the influence of geochemical features on the mechanical properties of
375 organic matter is investigated by combining various geochemical and micromechanical
376 characterization methods. The relations between the mechanical properties of different organic
377 types and thermal maturities are summarized in Figure 8. The main findings are as follows:

(1) Inertinite, vitrinite, and bitumen show different image features under the oil immersion objective and have a different reflectance range. It is difficult to distinguish organic type only according to the image contrast of SEM images.

(2) The vitrinite reflectance of the four shale samples is from 0.62% to 1.13%. With the same thermal maturity, mechanical heterogeneity exists within different types of organic matter. Inertinite has the highest Young's modulus, while the modulus of bitumen is the lowest. Taking sample J3 as an example, the Young's modulus of inertinite is more than two times that of the modulus of bitumen.

(3) The Young's moduli of all types of organic matter increase with thermal maturity. When vitrinite reflectance increases from 0.62% to 1.13%, the Young's modulus of inertinite increases from 5.29 GPa to 8.32 GPa, by 57%, and the Young's modulus of vitrinite increases from 3.57 GPa to 6.35 GPa, by 78%. The indentation creep calculation results suggest that the stiffer organic type indicates less creep influence.

(4) Characteristic peaks of carbon material can be found in the Raman spectrum of inertinite. The intensity ratio of D peak to G peak exhibits a decreasing trend with thermal maturity, indicating the increase of graphitization degree of organic matter.

(5) The geochemical and micromechanical characterization results reveal that the mechanical properties of organic matter are influenced by both organic type and thermal maturity. Compared with bitumen, vitrinite and inertinite have more polycyclic aromatic hydrocarbons, fewer saturated aliphatic hydrocarbons, and higher carbon content. Therefore, with the same thermal maturity, the Young's modulus of vitrinite and inertinite is higher than that of bitumen. With the increase of thermal maturity, the aliphatic structure is gradually decomposed and consumed, and

400 the aromaticity of kerogen increases. Consequently, IR (D/G) decreases, and the Young's
401 modulus increases.
402 (6) The mechanical behavior of organic matter plays an important role in the predictions of
403 macroscopic mechanical properties at the core scale and even the well scale, especially for
404 organic-rich shales. This can be done based on upscaling methods, such as the Mori-Tanaka
405 model and the self-consistence method, with the mechanical characterization results of the main
406 constituents in shale (Abedi et al., 2016; Goodarzi et al., 2017; Zhao et al., 2018). The
407 characterization in this work can serve as a supplement to micro constituent input databases for
408 more reliable overall calculation results. At micro scale, the experimental research can also
409 provide validation for related molecular simulations (Bousige et al., 2016; Wu and Firoozabadi,
410 2020). In addition, mechanical variation within organic matters has the potential to inversely
411 assist with the identification of organic type and the determination of thermal maturity.

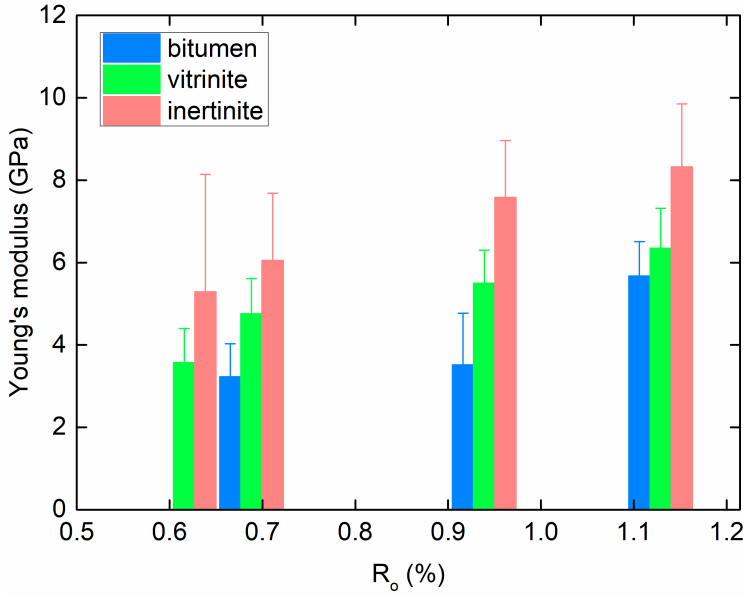

412

413 **Figure 8.** Young's modulus of organic matter with different vitrinite reflectance.

414 Considering sample-to-sample variation, this work proposes a workflow focusing on fixed
415 micro areas for different characterization. The data volume is also significantly increased

compared with that in the extant literature. However, the range of vitrinite reflectance in this study is limited, and all of the four samples are in the mature stage. In the future, shale samples in other thermal maturation stages need to be investigated.

Acknowledgements

This work is partially funded by the National Natural Science Foundation of China (Grant No. 51520105005 and U1663208) and the National Science and Technology Major Project of China (Grant No. 2016ZX05034001-007, 2017ZX05009-005, and 2017ZX05049-003). The data used in this paper are available through the following link: http://dx.doi.org/10.17632/hh22sgnnv4.1.

References

Abedi, S., Slim, M., & Ulm, F.-J. (2016). Nanomechanics of organic-rich shales: the role of thermal maturity and organic matter content on texture. *Acta Geotechnica*, *11*(4), 775-787. https://doi.org/10.1007/s11440-016-0476-2

Ahmadov, R., Vanorio, T., & Mavko, G. (2009). Confocal laser scanning and atomic-force microscopy in estimation of elastic properties of the organic-rich Bazhenov Formation. *The Leading Edge*, *28*(1), 18-23. https://doi.org/10.1190/1.3064141

Alstadt, K. N., Katti, K. S., & Katti, D. R. (2015). Nanoscale morphology of kerogen and in situ nanomechanical properties of green river oil shale. *Journal of Nanomechanics and Micromechanics*, *6*(1), 04015003. https://doi.org/10.1061/(ASCE)NM.2153-5477.0000103

Balooch, G., Marshall, G., Marshall, S., Warren, O., Asif, S. S., & Balooch, M. (2004). Evaluation of a new modulus mapping technique to investigate microstructural features of human teeth. *Journal of Biomechanics*, *37*(8), 1223-1232. https://doi.org/10.1016/j.jbiomech.2003.12.012

Bennett, K. C., Berla, L. A., Nix, W. D., & Borja, R. I. (2015). Instrumented nanoindentation and 3D mechanistic modeling of a shale at multiple scales. *Acta Geotechnica*, *10*(1), 1-14. https://doi.org/10.1007/s11440-014-0363-7

Bertrand, R. (1990). Correlations among the reflectances of vitrinite, chitinozoans, graptolites and scolecodonts. *Organic Geochemistry*, *15*(6), 565-574. https://doi.org/10.1016/0146-6380(90)90102-6

442 Bertrand, R., & Heroux, Y. (1987). Chitinozoan, graptolite, and scolecodont reflectance as an alternative to vitrinite
443 and pyrobitumen reflectance in Ordovician and Silurian strata, Anticosti Island, Quebec, Canada. *AAPG Bulletin*,
444 *71*(8), 951-957. https://doi.org/10.1306/948878f7-1704-11d7-8645000102c1865d
445 Borodich, F. M., Bull, S., & Epshtein, S. (2015). Nanoindentation in studying mechanical properties of
446 heterogeneous materials. *Journal of Mining Science*, *51*(3), 470-476. https://doi.org/10.1134/s1062739115030072
447 Bousige, C., Ghimbeu, C. M., Vix-Guterl, C., Pomerantz, A. E., Suleimenova, A., Vaughan, G., Garbarino, G.,
448 Feygenson, M., Wildgruber, C., & Ulm, F.-J. (2016). Realistic molecular model of kerogen's nanostructure. *Nature*
449 *Materials*, *15*(5), 576-582. https://doi.org/10.1038/nmat4541
450 Chagnon, L., Arnold, G., Giljean, S., & Brogly, M. (2013). Elastic recovery and creep properties of waterborne two-
451 component polyurethanes investigated by micro-indentation. *Progress in Organic Coatings*, *76*(10), 1337-1345.
452 https://doi.org/10.1016/j.porgcoat.2013.04.003
453 Craddock, P. R., Bake, K. D., & Pomerantz, A. E. (2018). Chemical, molecular, and microstructural evolution of
454 kerogen during thermal maturation: case study from the Woodford Shale of Oklahoma. *Energy & Fuels*, *32*(4),
455 4859-4872. https://doi.org/10.1021/acs.energyfuels.8b00189
456 Cudjoe, S., Vinassa, M., Gomes, J. H. B., & Barati, R. G. (2016). A comprehensive approach to sweet-spot mapping
457 for hydraulic fracturing and CO2 huff-n-puff injection in Chattanooga shale formation. *Journal of Natural Gas*
458 *Science and Engineering*, *33*, 1201-1218. https://doi.org/10.1016/j.jngse.2016.03.042
459 Dayal, P., Savvides, N., & Hoffman, M. (2009). Characterisation of nanolayered aluminium/palladium thin films
460 using nanoindentation. *Thin Solid Films*, *517*(13), 3698-3703. https://doi.org/10.1016/j.tsf.2009.01.174
461 Dokukin, M. E., & Sokolov, I. (2012). Quantitative mapping of the elastic modulus of soft materials with HarmoniX
462 and PeakForce QNM AFM modes. *Langmuir*, *28*(46), 16060-16071. https://doi.org/10.1021/la302706b
463 Dresselhaus, M. S., Dresselhaus, G., Saito, R., & Jorio, A. (2005). Raman spectroscopy of carbon nanotubes.
464 *Physics Reports*, *409*(2), 47-99. https://doi.org/10.1016/j.physrep.2004.10.006
465 Duan, D., Zhang, D., Ma, X., Yang, Y., Ran, Y., & Mao, J. (2018). Chemical and structural characterization of
466 thermally simulated kerogen and its relationship with microporosity. *Marine and Petroleum Geology*, *89*, 4-13.
467 https://doi.org/10.1016/j.marpetgeo.2016.12.016
468 Eliyahu, M., Emmanuel, S., Day-Stirrat, R. J., & Macaulay, C. I. (2015). Mechanical properties of organic matter in
469 shales mapped at the nanometer scale. *Marine and Petroleum Geology*, *59*, 294-304.

https://doi.org/10.1016/j.marpetgeo.2014.09.007

Emmanuel, S., Eliyahu, M., Day-Stirrat, R. J., Hofmann, R., & Macaulay, C. I. (2016). Impact of thermal maturation on nano-scale elastic properties of organic matter in shales. *Marine and Petroleum Geology*, *70*, 175-184. https://doi.org/10.1016/j.marpetgeo.2015.12.001

Epshtein, S. A., Borodich, F. M., & Bull, S. J. (2015). Evaluation of elastic modulus and hardness of highly inhomogeneous materials by nanoindentation. *Applied Physics A*, *119*(1), 325-335. https://doi.org/10.1007/s00339-014-8971-5

Ferrari, A. C., Meyer, J., Scardaci, V., Casiraghi, C., Lazzeri, M., Mauri, F., Piscanec, S., Jiang, D., Novoselov, K., & Roth, S. (2006). Raman spectrum of graphene and graphene layers. *Physical Review Letters*, *97*(18), 187401. https://doi.org/10.1103/PhysRevLett.97.187401

Goodarzi, M., Rouainia, M., Aplin, A., Cubillas, P., & de Block, M. (2017). Predicting the elastic response of organic-rich shale using nanoscale measurements and homogenisation methods. *Geophysical Prospecting*. https://doi.org/10.1111/1365-2478.12475

Hunt, J. M. (1979). *Petroleum geochemistry and geology*. W H Freemme and Company, San Francisco.

Hutton, A., Bharati, S., & Robl, T. (1994). Chemical and petrographic classification of kerogen/macerals. *Energy & Fuels*, *8*(6), 1478-1488. https://doi.org/10.1021/ef00048a038

ISO14577-1 (2002). *Metallic materials—instrumented indentation test for hardness and materials parameters.* International Organization for Standardization, Geneva.

Jacob, H. (1989). Classification, structure, genesis and practical importance of natural solid oil bitumen ("migrabitumen"). *International Journal of Coal Geology*, *11*(1), 65-79. https://doi.org/10.1016/0166-5162(89)90113-4

Jiu, K., Ding, W., Huang, W., You, S., Zhang, Y., & Zeng, W. (2013). Simulation of paleotectonic stress fields within Paleogene shale reservoirs and prediction of favorable zones for fracture development within the Zhanhua Depression, Bohai Bay Basin, east China. *Journal of Petroleum Science and Engineering*, *110*, 119-131. https://doi.org/10.1016/j.petrol.2013.09.002

Johnson, K. L. (1987). *Contact mechanics*. Cambridge University Press.

Kelemen, S., & Fang, H. (2001). Maturity trends in Raman spectra from kerogen and coal. *Energy & Fuels*, *15*(3), 653-658. https://doi.org/10.1021/ef0002039

Koch, T., Kogler, F. R., Schubert, U., & Seidler, S. (2007). Mechanical properties of organic-inorganic hybrid materials determined by indentation techniques. *Monatshefte für Chemie-Chemical Monthly*, *138*(4), 293-299. https://doi.org/10.1007/s00706-007-0612-7

Kumar, V., Sondergeld, C. H., & Rai, C. S. (2012). *Nano to macro mechanical characterization of shale*. Paper presented at SPE Annual Technical Conference and Exhibition, Society of Petroleum Engineers. https://doi.org/10.2118/159804-ms

Li, C., Ostadhassan, M., Gentzis, T., Kong, L., Carvajal-Ortiz, H., & Bubach, B. (2018). Nanomechanical characterization of organic matter in the Bakken formation by microscopy-based method. *Marine and Petroleum Geology*, *96*, 128-138. https://doi.org/10.1016/j.marpetgeo.2018.05.019

Liu, Y., Xiong, Y., Liu, K., Yang, C., & Peng, P. (2019). Indentation size and loading rate sensitivities on mechanical properties and creep behavior of solid bitumen. *International Journal of Coal Geology*, *216*, 103295. https://doi.org/10.1016/j.coal.2019.103295

Lünsdorf, N. K. (2016). Raman spectroscopy of dispersed vitrinite—Methodical aspects and correlation with reflectance. *International Journal of Coal Geology*, *153*, 75-86. https://doi.org/10.1016/j.coal.2015.11.010

Naizhen, L., & Guoyong, W. (2016). Shale gas sweet spot identification and precise geo-steering drilling in Weiyuan Block of Sichuan Basin, SW China. *Petroleum Exploration and Development*, *43*(6), 1067-1075. https://doi.org/10.1016/S1876-3804(16)30124-0

Oliver, W. C., & Pharr, G. M. (1992). An improved technique for determining hardness and elastic modulus using load and displacement sensing indentation experiments. *Journal of Materials Research*, *7*(06), 1564-1583. https://doi.org/10.1557/jmr.1992.1564

Oliver, W. C., & Pharr, G. M. (2004). Measurement of hardness and elastic modulus by instrumented indentation: Advances in understanding and refinements to methodology. *Journal of Materials Research*, *19*(1), 3-20. https://doi.org/10.1557/jmr.2004.19.1.3

Pharr, G., Oliver, W., & Brotzen, F. (1992). On the generality of the relationship among contact stiffness, contact area, and elastic modulus during indentation. *Journal of Materials Research*, *7*(3), 613-617. https://doi.org/10.1557/JMR.1992.0613

Pimenta, M., Dresselhaus, G., Dresselhaus, M. S., Cancado, L., Jorio, A., & Saito, R. (2007). Studying disorder in graphite-based systems by Raman spectroscopy. *Physical Chemistry Chemical Physics*, *9*(11), 1276-1290.

http://dx.doi.org/10.1039/B613962K

Rybacki, E., Meier, T., & Dresen, G. (2016). What controls the mechanical properties of shale rocks?–Part II: Brittleness. *Journal of Petroleum Science and Engineering*, *144*, 39-58. https://doi.org/10.1016/j.petrol.2016.02.022

Stach, E., Murchison, D., Taylor, G. H., & Zierke, F. (1982). *Stach's textbook of coal petrology*. Borntraeger Berlin.

Syed Asif, S., Wahl, K., Colton, R., & Warren, O. (2001). Quantitative imaging of nanoscale mechanical properties using hybrid nanoindentation and force modulation. *Journal of Applied Physics*, *90*(3), 1192-1200. https://doi.org/10.1063/1.1380218

Tissot, B. P., & Welte, D. H. (2013). *Petroleum formation and occurrence*. Springer Science & Business Media.

Tong, J., Jiang, X., Han, X., & Wang, X. (2016). Evaluation of the macromolecular structure of Huadian oil shale kerogen using molecular modeling. *Fuel*, *181*, 330-339. https://doi.org/10.1016/j.fuel.2016.04.139

Tselev, A., Ivanov, I. N., Lavrik, N. V., Belianinov, A., Jesse, S., Mathews, J. P., Mitchell, G. D., & Kalinin, S. V. (2014). Mapping internal structure of coal by confocal micro-Raman spectroscopy and scanning microwave microscopy. *Fuel*, *126*, 32-37. https://doi.org/10.1016/j.fuel.2014.02.029

Ungerer, P., Collell, J., & Yiannourakou, M. (2014). Molecular modeling of the volumetric and thermodynamic properties of kerogen: Influence of organic type and maturity. *Energy & Fuels*, *29*(1), 91-105. https://doi.org/10.1021/ef502154k

Vranjes, S., Misch, D., Schöberl, T., Kiener, D., Gross, D., & Sachsenhofer, R. F. (2018). Nanoindentation study of macerals in coals from the Ukrainian Donets Basin. *Advances in Geosciences*, *45*. https://doi.org/10.5194/adgeo-45-73-2018

Wang, G., & Carr, T. R. (2012). Methodology of organic-rich shale lithofacies identification and prediction: A case study from Marcellus Shale in the Appalachian basin. *Computers & Geosciences*, *49*, 151-163. https://doi.org/10.1016/j.cageo.2012.07.011

Wang, M., Sherwood, N., Li, Z., Lu, S., Wang, W., Huang, A., Peng, J., & Lu, K. (2015). Shale oil occurring between salt intervals in the Dongpu Depression, Bohai Bay Basin, China. *International Journal of Coal Geology*, *152*, 100-112. https://doi.org/10.1016/j.coal.2015.07.004

Wilkins, R. W., Boudou, R., Sherwood, N., & Xiao, X. (2014). Thermal maturity evaluation from inertinites by Raman spectroscopy: the 'RaMM' technique. *International Journal of Coal Geology*, *128*, 143-152. https://doi.org/10.1016/j.coal.2014.03.006

554 Wilkinson, T. M., Zargari, S., Prasad, M., & Packard, C. E. (2015). Optimizing nano-dynamic mechanical analysis
555 for high-resolution, elastic modulus mapping in organic-rich shales. *Journal of Materials Science*, *50*(3), 1041-1049.
556 https://doi.org/10.1007/s10853-014-8682-5
557 Wu, T., & Firoozabadi, A. (2020). Mechanical properties and failure envelope of kerogen matrix by molecular
558 dynamics simulations. *The Journal of Physical Chemistry C*. https://doi.org/10.1021/acs.jpcc.9b09639
559 Yang, J., Hatcherian, J., Hackley, P. C., & Pomerantz, A. E. (2017). Nanoscale geochemical and geomechanical
560 characterization of organic matter in shale. *Nature Communications*, *8*(1), 2179. https://doi.org/10.1038/s41467-017-
561 02254-0
562 Zargari, S., Prasad, M., Mba, K. C., & Mattson, E. D. (2013). Organic maturity, elastic properties, and textural
563 characteristics of self resourcing reservoirs. *Geophysics*, *78*(4), D223-D235. https://doi.org/10.1190/geo2012-0431.1
564 Zargari, S., Wilkinson, T. M., Packard, C. E., & Prasad, M. (2016). Effect of thermal maturity on elastic properties
565 of kerogen. *Geophysics*, *81*(2), M1-M6. https://doi.org/10.1190/geo2015-0194.1
566 Zeszotarski, J. C., Chromik, R. R., Vinci, R. P., Messmer, M. C., Michels, R., & Larsen, J. W. (2004). Imaging and
567 mechanical property measurements of kerogen via nanoindentation. *Geochimica et Cosmochimica Acta*, *68*(20),
568 4113-4119. https://doi.org/10.1016/j.gca.2003.11.031
569 Zhang, Y., Lebedev, M., Smith, G., Jing, Y., Busch, A., & Iglauer, S. (2019). Nano-mechanical properties and pore-
570 scale characterization of different rank coals. *Natural Resources Research*, 1-14. https://doi.org/10.1007/s11053-
571 019-09572-8
572 Zhao, J., Zhang, D., Wu, T., Tang, H., Xuan, Q., Jiang, Z., & Dai, C. (2018). Multiscale approach for mechanical
573 characterization of organic-rich shale and its application. *International Journal of Geomechanics*, *19*(1), 04018180.
574 https://doi.org/10.1061/(asce)gm.1943-5622.0001281
575

Figure 1.

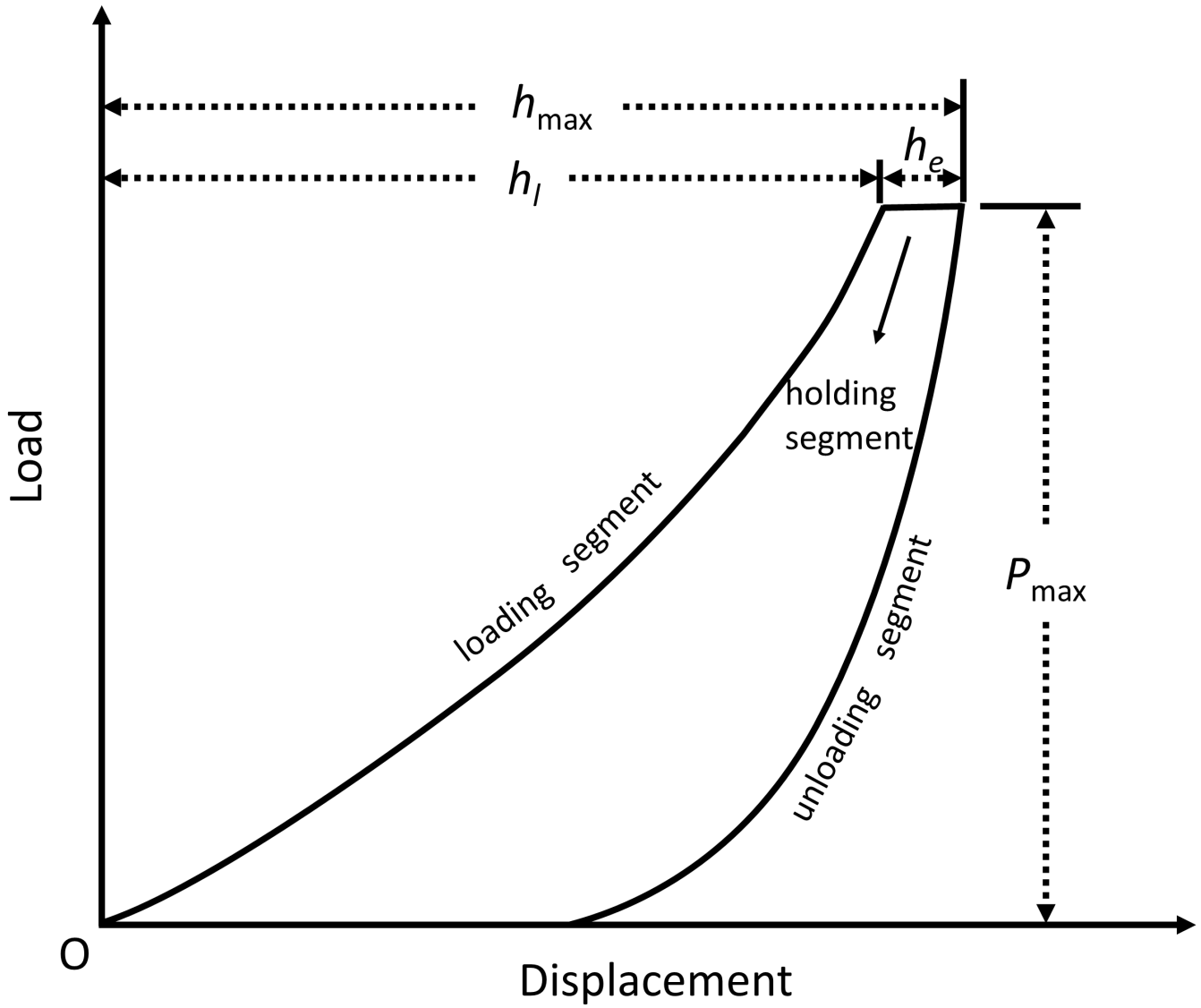
h_{max}
h_e
h_l
holding segment
loading segment
unloading segment
P_{max}
Load
O
Displacement

Figure 2.

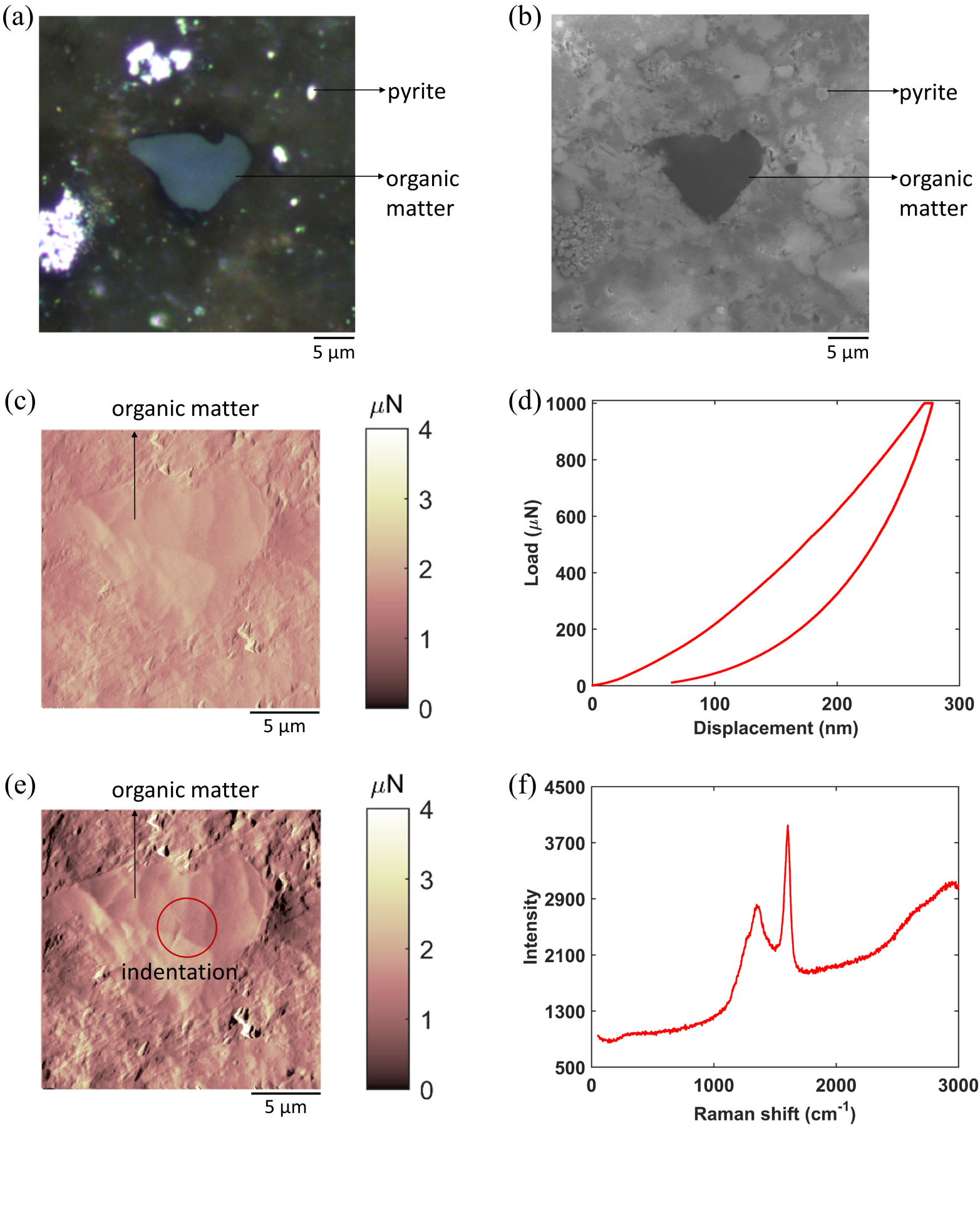
(a)
pyrite
organic matter
5 µm
(b)
pyrite
organic matter
5 µm
(c)
organic matter
µN
4
3
2
1
0
5 µm
(d)
Load (µN)
1000
800
600
400
200
0
0
100
200
300
Displacement (nm)
(e)
organic matter
indentation
µN
4
3
2
1
0
5 µm
(f)
Intensity
4500
3700
2900
2100
1300
500
0
1000
2000
3000
Raman shift (cm-1)

Figure 3.

(a)

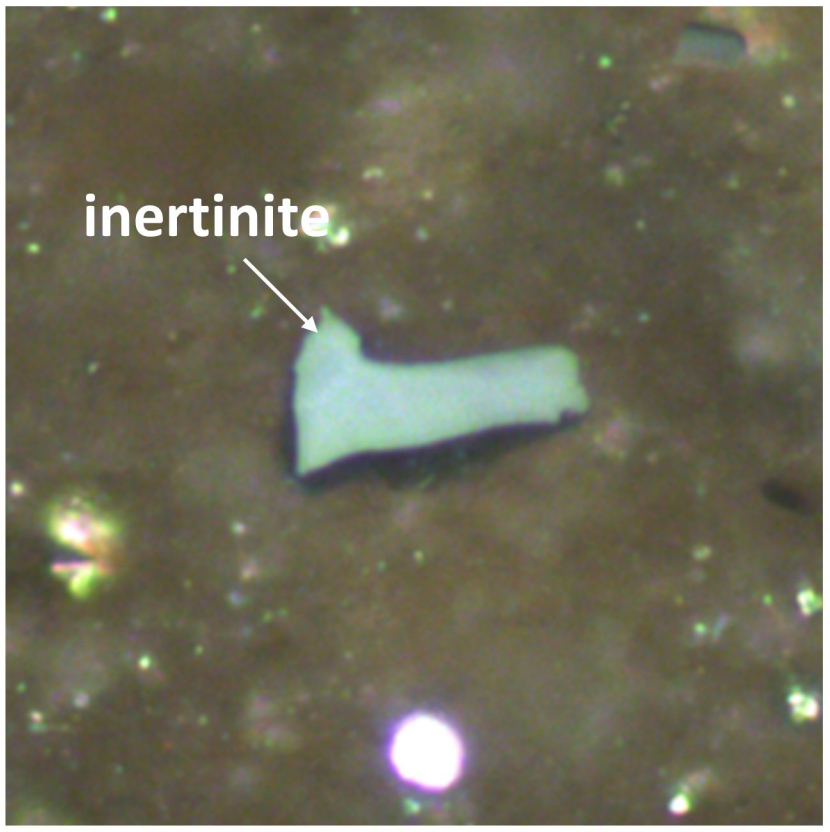
inertinite
10 µm

(b)

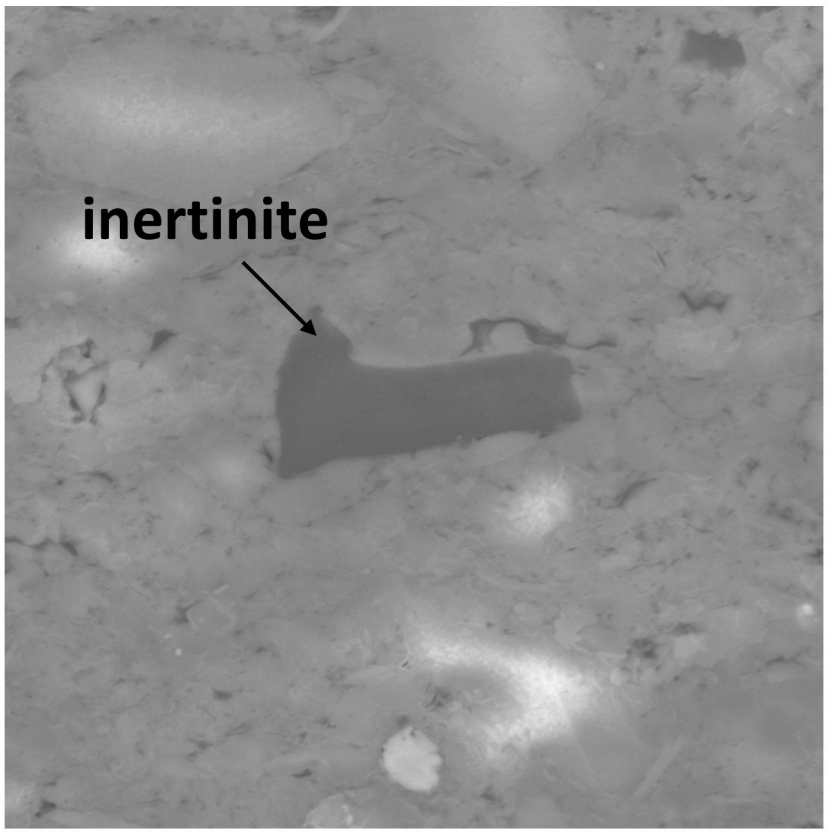
inertinite
10 µm

(c)

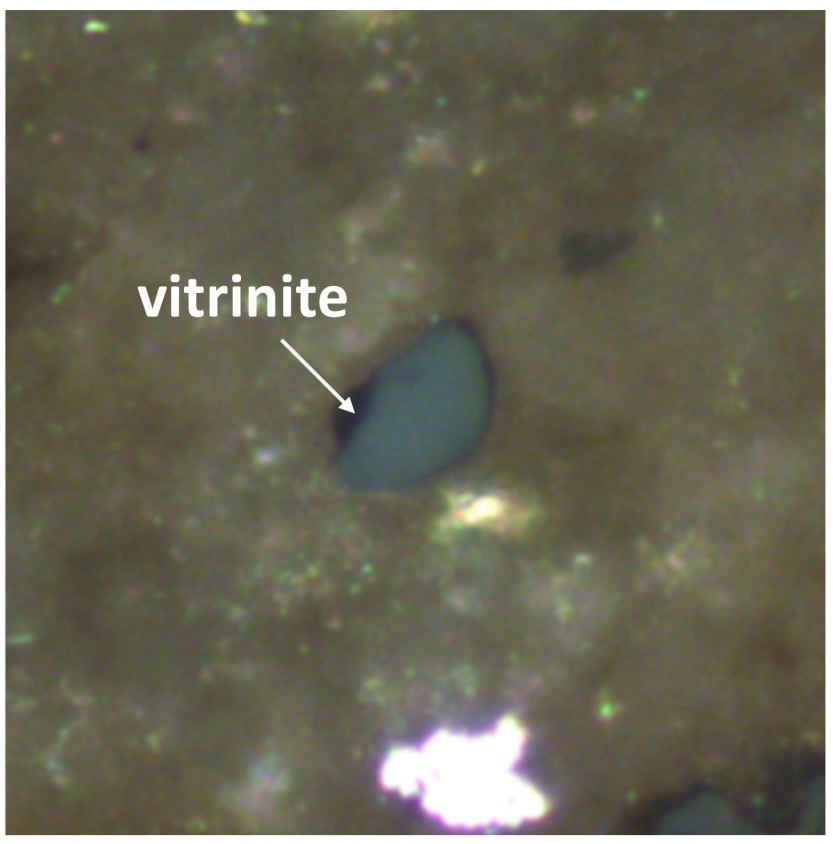
vitrinite
10 µm

(d)

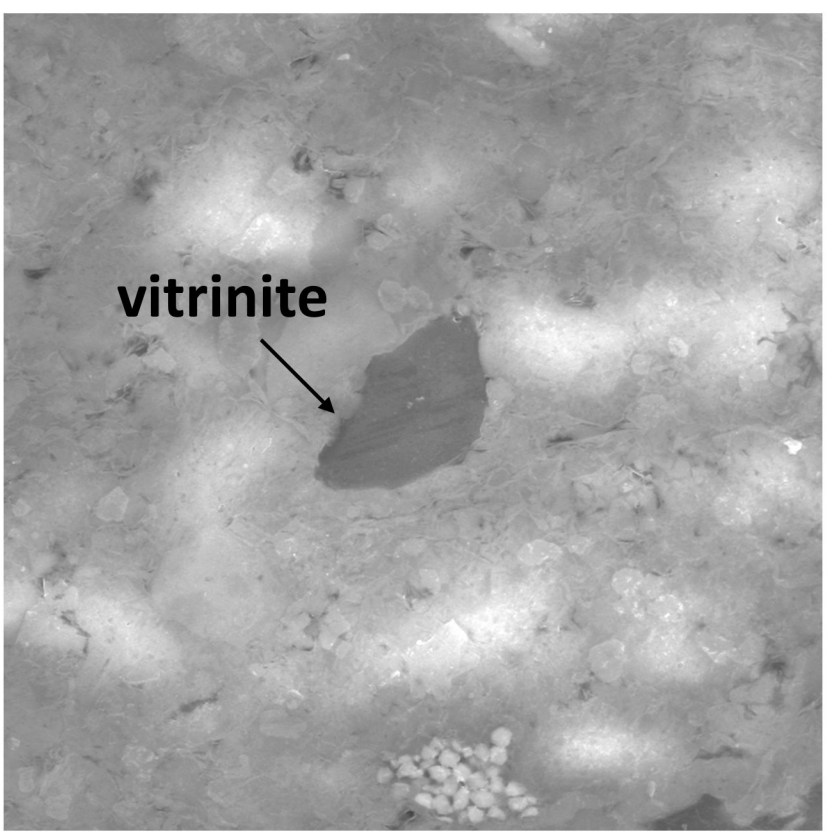
vitrinite
10 µm

(e)

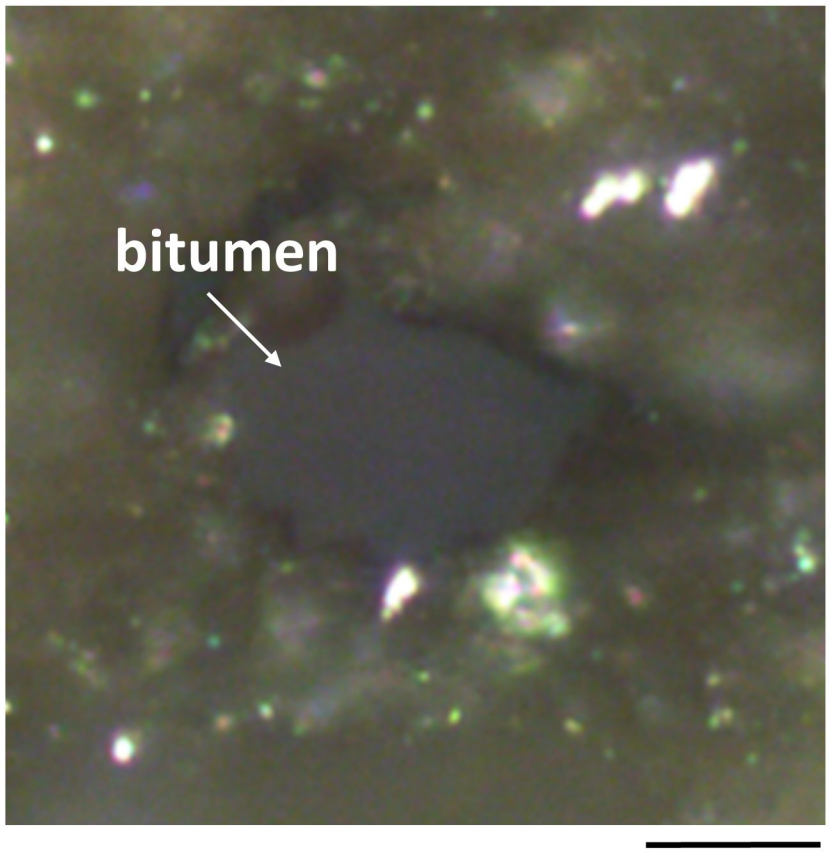
bitumen
10 µm

(f)

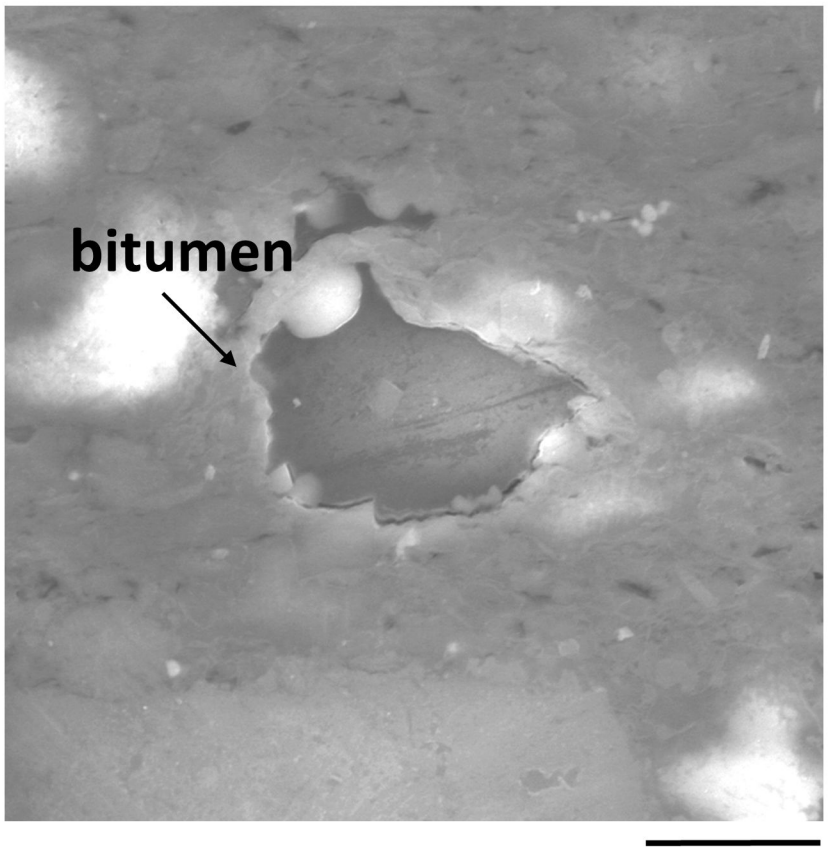
bitumen
10 µm

Figure 4.

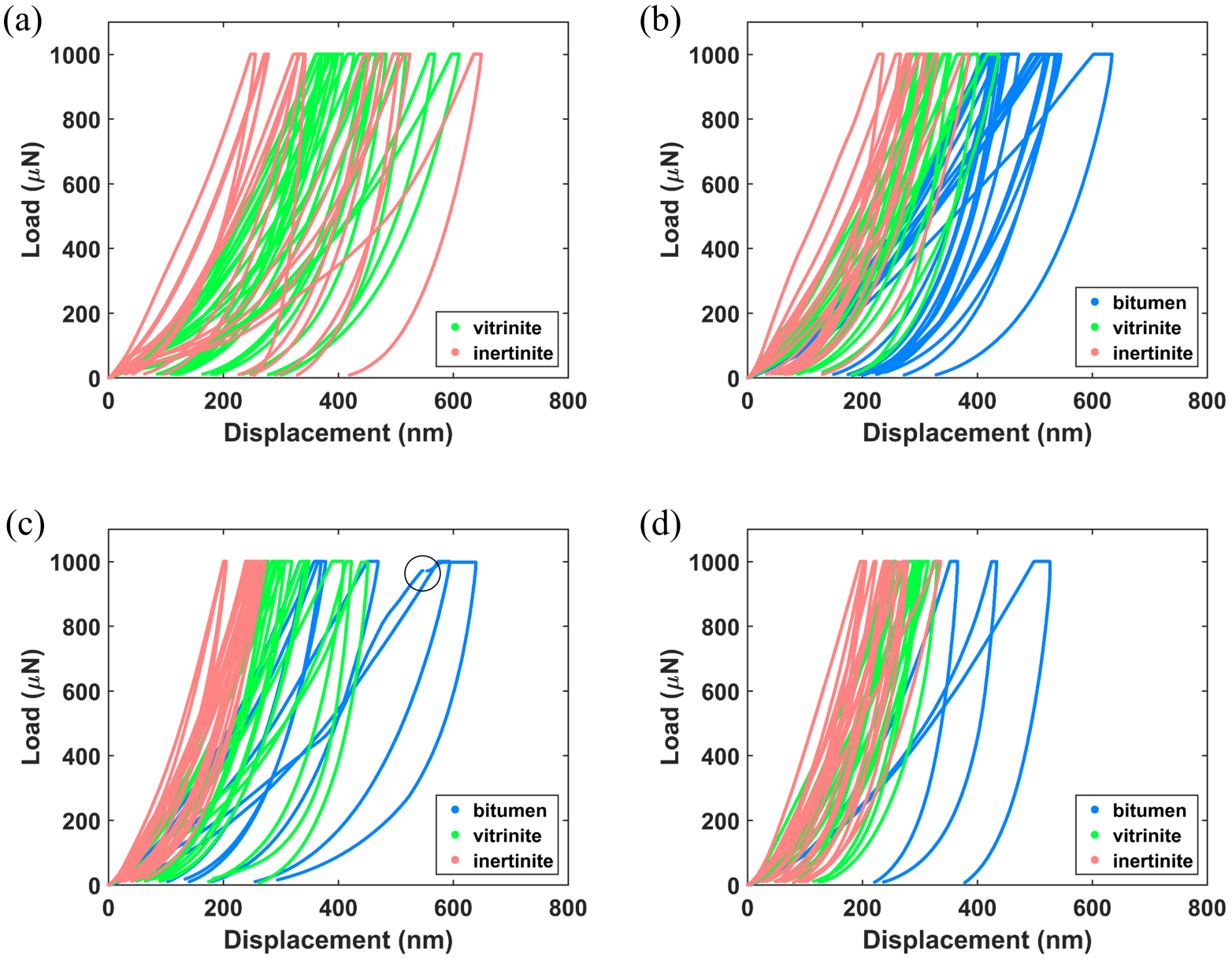
(a)
Load (μN)
Displacement (nm)
vitrinite
inertinite
(b)
Load (μN)
Displacement (nm)
bitumen
vitrinite
inertinite
(c)
Load (μN)
Displacement (nm)
bitumen
vitrinite
inertinite
(d)
Load (μN)
Displacement (nm)
bitumen
vitrinite
inertinite

Figure 5.

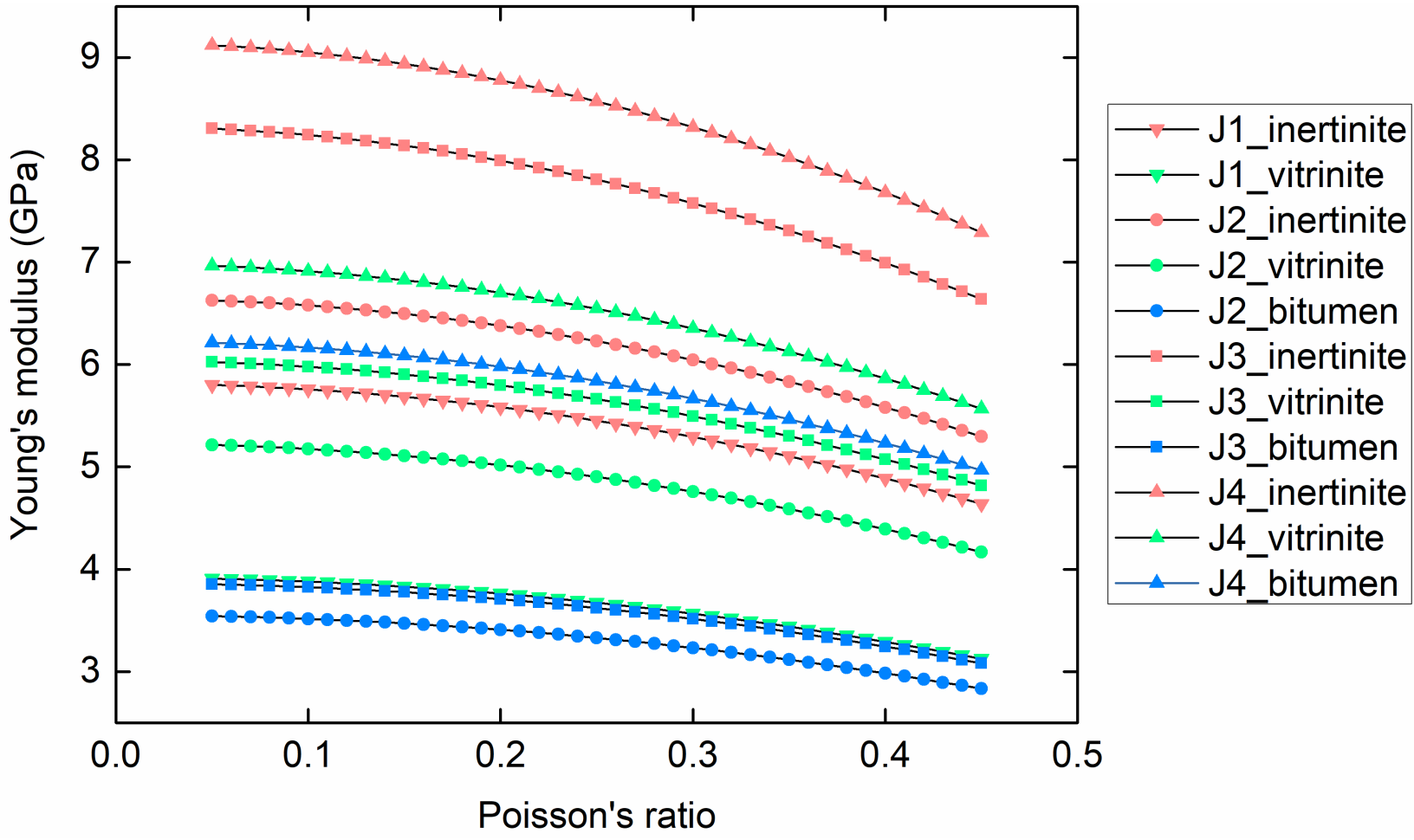
Young's modulus (GPa)
9
8
7
6
5
4
3
0.0
0.1
0.2
0.3
0.4
0.5
Poisson's ratio
J1_inertinite
J1_vitrinite
J2_inertinite
J2_vitrinite
J2_bitumen
J3_inertinite
J3_vitrinite
J3_bitumen
J4_inertinite
J4_vitrinite
J4_bitumen

Figure 6.

(a)

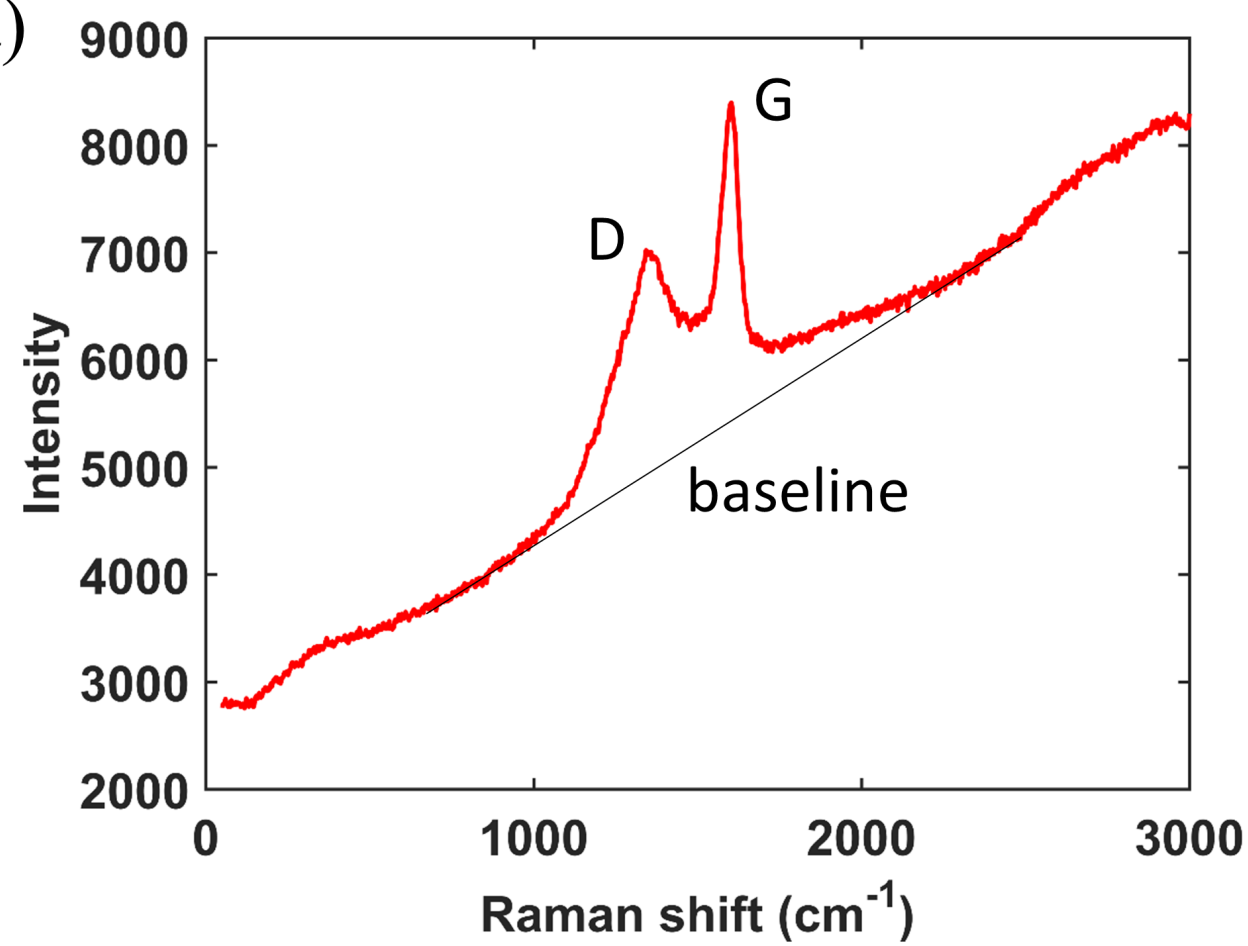
9000
8000
7000
6000
5000
4000
3000
2000
Intensity
G
D
baseline
0
1000
2000
3000
Raman shift (cm-1)

(b)

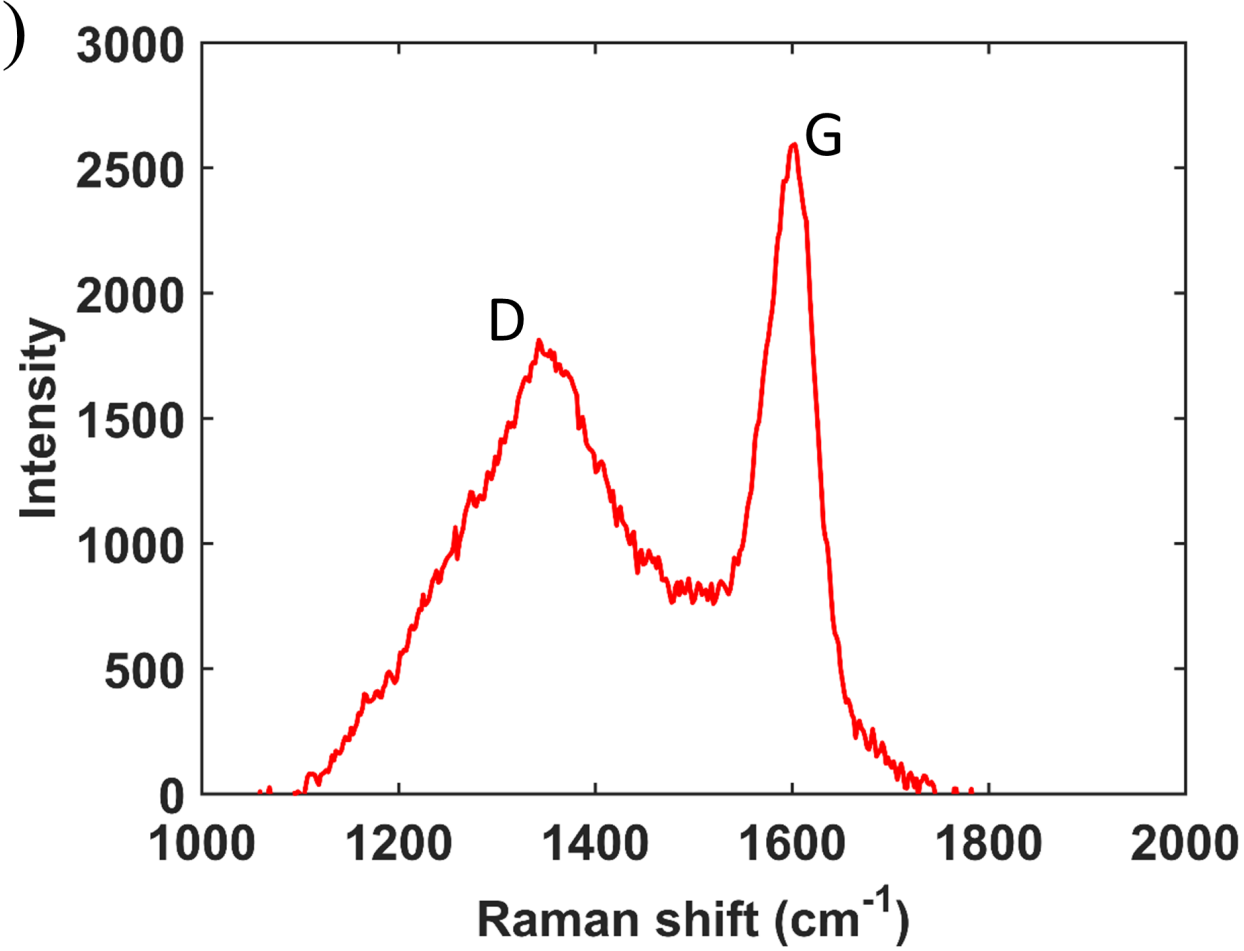
3000
2500
2000
1500
1000
500
0
Intensity
G
D
1000
1200
1400
1600
1800
2000
Raman shift (cm-1)

Figure 7.

(a)

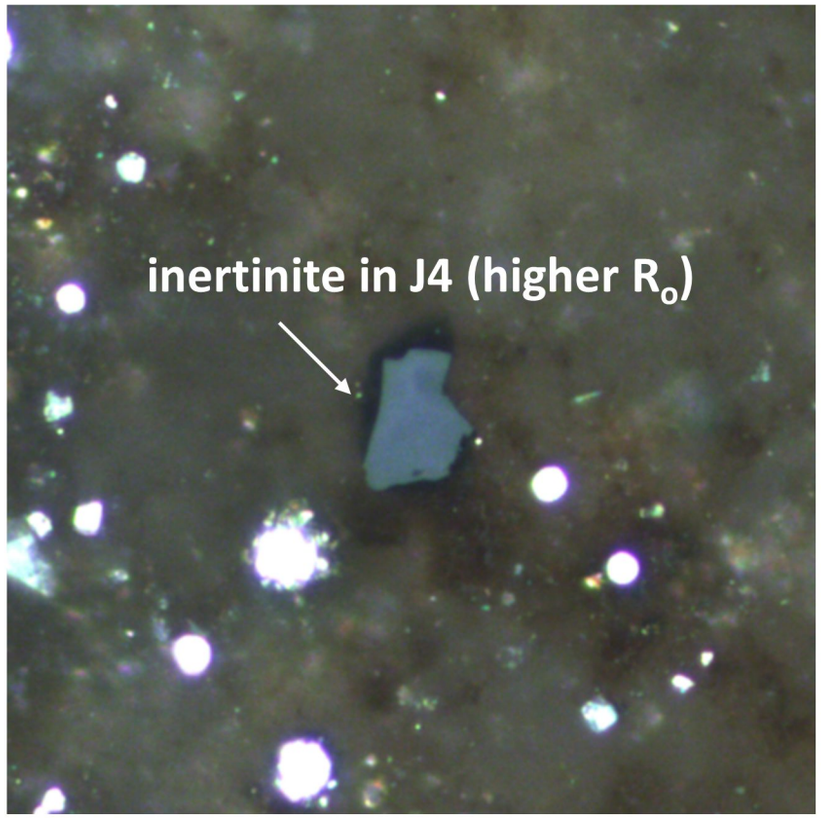
inertinite in J4 (higher R_o)
10 μm

(b)

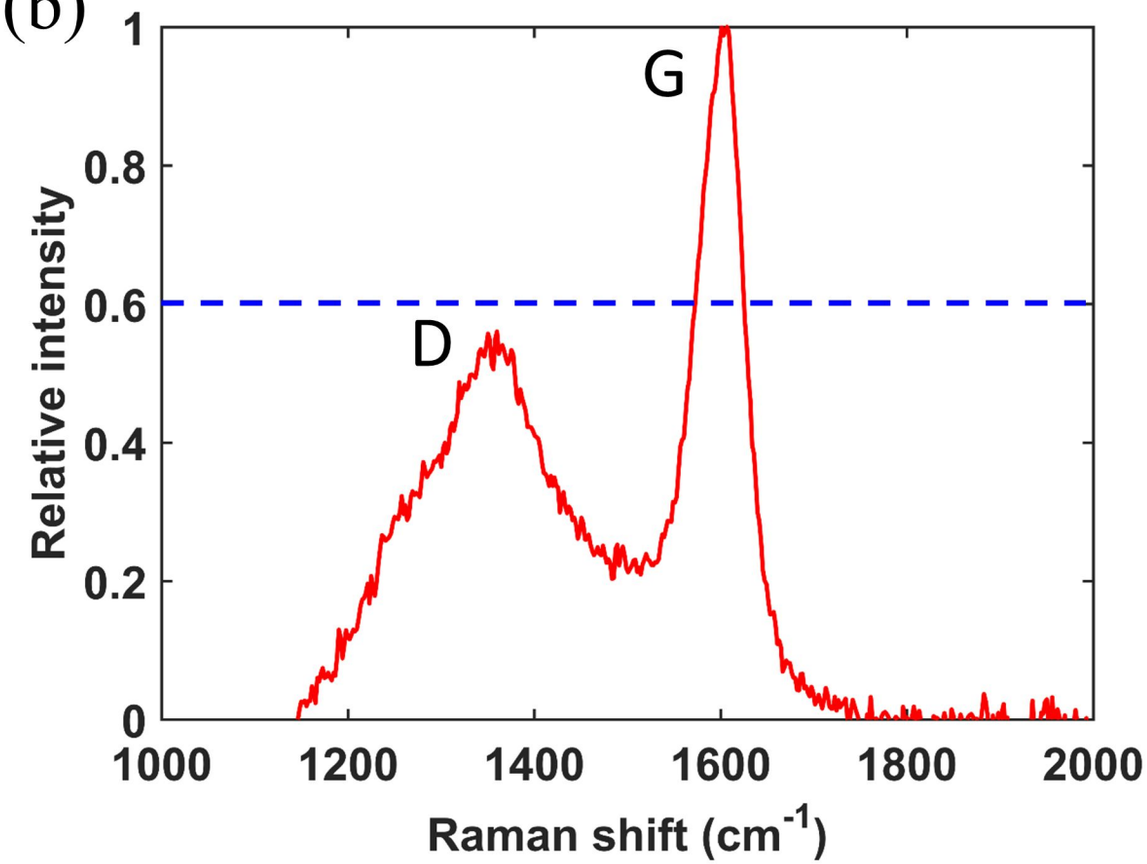
G
D
Relative intensity
Raman shift (cm-1)
0
0.2
0.4
0.6
0.8
1
1000
1200
1400
1600
1800
2000

(c)

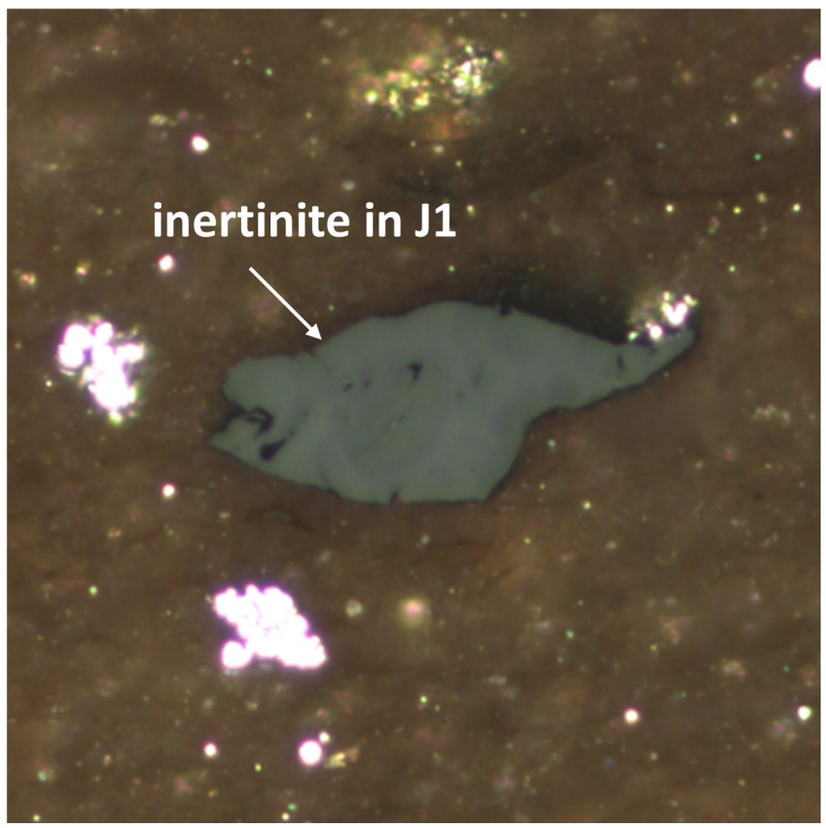
inertinite in J1
10 μm

(d)

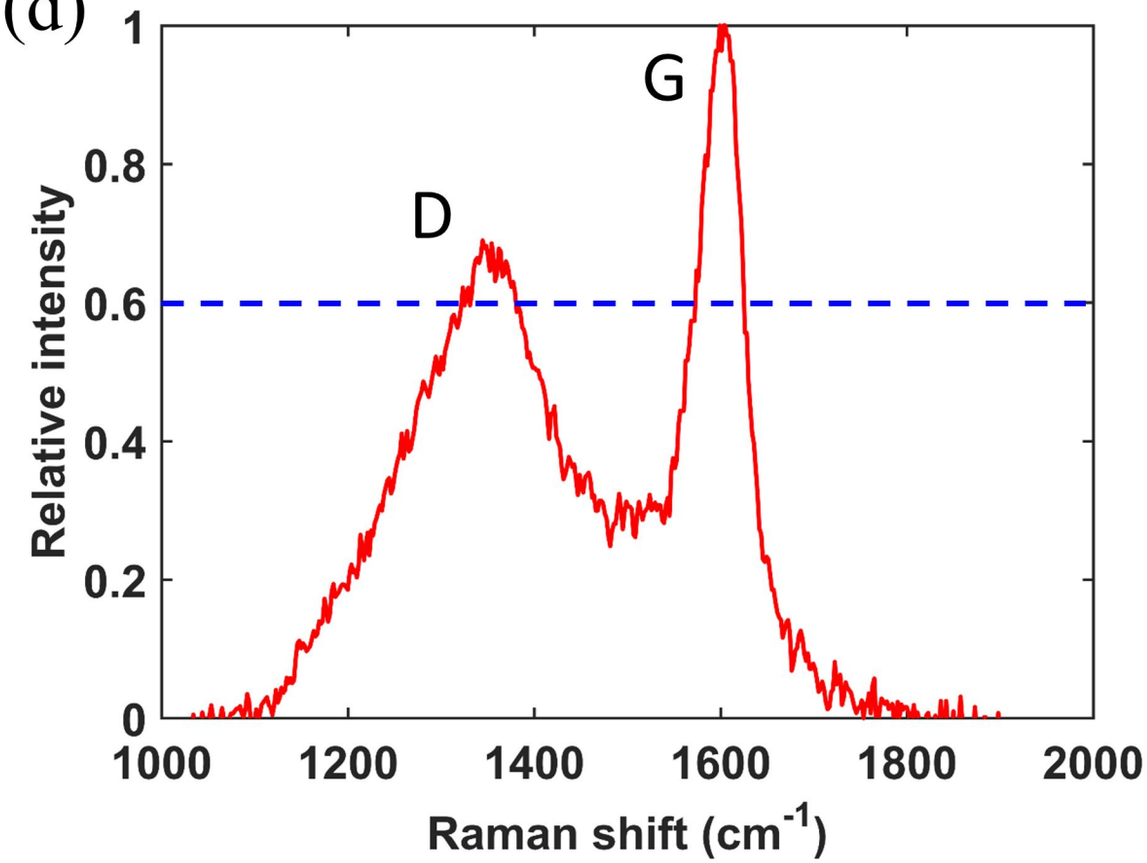
G
D
Relative intensity
Raman shift (cm-1)
0
0.2
0.4
0.6
0.8
1
1000
1200
1400
1600
1800
2000

Figure 8.

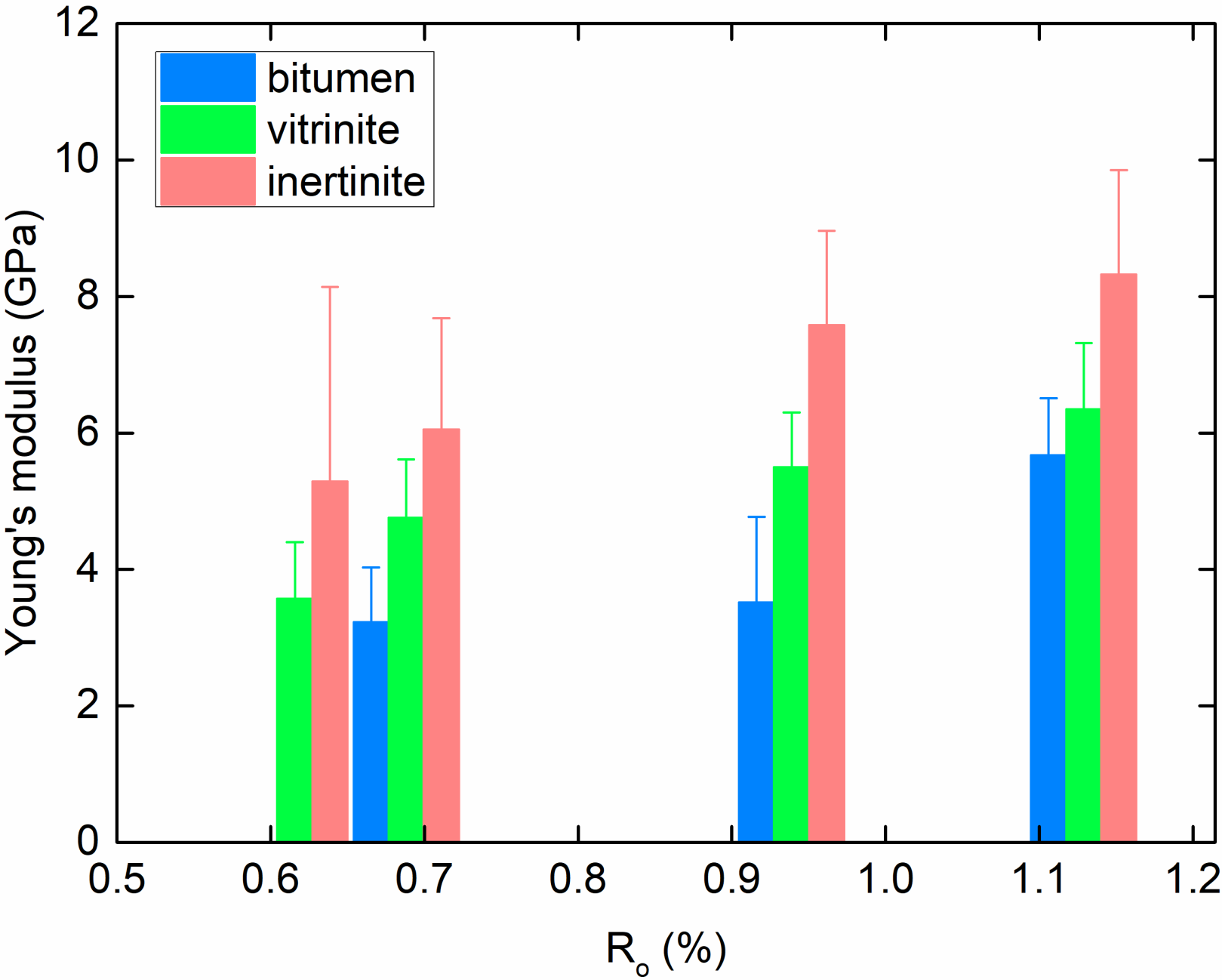
bitumen
vitrinite
inertinite
Young's modulus (GPa)
0
2
4
6
8
10
12
0.5
0.6
0.7
0.8
0.9
1.0
1.1
1.2
R$_o$ (%)